ACS APPLIED MATERIALS & INTERFACES

Subscriber access provided by Uppsala universitetsbibliotek

Biological and Medical Applications of Materials and Interfaces

MoS2-ReS2 Heterojunctions from a Bimetallic Co-chamber Feeding Atomic Layer Deposition for Ultrasensitive MiRNA-21 Detection

Lei Liu, Kejian Ma, Xiaoxuan Xu, Shangguan Changjian,
Jun Lv, Songyang Zhu, Songlong Jiao, and Jianqiao Wang

ACS Appl. Mater. Interfaces, **Just Accepted Manuscript** • DOI: 10.1021/acsami.0c07145 • Publication Date (Web): 03 Jun 2020

Downloaded from pubs.acs.org on June 4, 2020

Just Accepted

"Just Accepted" manuscripts have been peer-reviewed and accepted for publication. They are posted online prior to technical editing, formatting for publication and author proofing. The American Chemical Society provides "Just Accepted" as a service to the research community to expedite the dissemination of scientific material as soon as possible after acceptance. "Just Accepted" manuscripts appear in full in PDF format accompanied by an HTML abstract. "Just Accepted" manuscripts have been fully peer reviewed, but should not be considered the official version of record. They are citable by the Digital Object Identifier (DOI®). "Just Accepted" is an optional service offered to authors. Therefore, the "Just Accepted" Web site may not include all articles that will be published in the journal. After a manuscript is technically edited and formatted, it will be removed from the "Just Accepted" Web site and published as an ASAP article. Note that technical editing may introduce minor changes to the manuscript text and/or graphics which could affect content, and all legal disclaimers and ethical guidelines that apply to the journal pertain. ACS cannot be held responsible for errors or consequences arising from the use of information contained in these "Just Accepted" manuscripts.

is published by the American Chemical Society. 1155 Sixteenth Street N.W., Washington, DC 20036

Published by American Chemical Society. Copyright © American Chemical Society. However, no copyright claim is made to original U.S. Government works, or works produced by employees of any Commonwealth realm Crown government in the course of their duties.

MoS_2-ReS_2 Heterojunctions from a Bimetallic Co-chamber Feeding Atomic Layer Deposition for Ultrasensitive MiRNA-21 Detection

Lei Liu[1, *, #], Kejian Ma[1, #], Xiaoxuan Xu[2, *], Changjian Shangguan[1], Jun Lv[1], Songyang Zhu[1], Songlong Jiao[1], Jianqiao Wang[1]

1. School of Mechanical Engineering, Southeast University, Nanjing 211189, P. R. China
2. Nanjing Institute of Industry Technology, Nanjing 210023, P. R. China

# These authors contributed equally to this work

* Corresponding author, email: liulei@seu.edu.cn; xuxx@niit.edu.cn

Abstract

Rhenium disulfide (ReS_2) which possessed a unique direct band gap from bulk to monolayer played a very important role in the establishing optoelectronic devices, while the rapid recombination of electron-hole pair might hinder its further applications. Therefore, in order to improve its photocurrent performance, a bimetallic co-chamber feeding atomic layer deposition (ALD) with a precise dose regulation strategy was used to fabricate MoS_2-ReS_2 heterojunctions with controllable Mo-to-Re ratio in this work. Furthermore, because of the controlled addition of Mo atoms, the electron transfer capacity, carrier mobility and photocurrent response of these heterojunctions were significantly improved, among which the sample obtained under 100 super cycles (one super cycle for this sample consists of the followings in turn: 1 $ReCl_5$ pulse, 1 H_2S pulse, 1 $ReCl_5$ pulse and 1 $MoCl_5$ pulse, 1 H_2S pulse, the real Mo-to-Re ratio R_r=57.9%) exhibited the best photocurrent response. Due to the significant improvement in optoelectronic performance, photoelectrochemical (PEC) biosensor with the basis of the above optimized sample could achieve ultrasensitive detection of cancer-related miRNA-21 ranging from 10 aM to 1 nM with a low detection limit of 2.8 aM.

Key words: ALD; heterojunctions; ReS_2; MoS_2; miRNA-21

1. Introduction

Rhenium disulfide (ReS_2), as a vibrant young member of the transition metal dichalcogenides, has been more and more widely concerned and investigated because of its unique anisotropic structure and direct band gap from bulk to monolayer.[1,2] In particular, ReS_2 possesses excellent biocompatibility, which renders ReS_2 to be widely employed in clinical and biomedical fields.[1] At the same time, its layer-independent features caused by weak interlayer coupling favors its application in electronics and optoelectronics.[3] However, the rapid recombination of electron-hole pairs and poor electronic transmission capacity in pure ReS_2 limited its wide applications.[4]

In order to overcome this deficiency, many efforts such as defect engineering, atom doping, heterostructure designing had been carried out to achieve modified ReS_2 materials with improved optoelectronic properties, while existed studies indicated that fewer-layer ReS_2 (2.5 nm ~ 4.5 nm) with natural n-doping possessed the highest photo responsivity than other individual 2-dimentianl (2-d) material.[5] Additionally, substitution doping had also been regarded as an effective way to adjust band structure and increase carrier concentration.[6,7] For Mo-doped ReS_2, it transferred from n-type to p-type semiconductor and the carrier concentration was improved with the substitution of Mo for Re.[8] Although mono-/fewer-layer products have been now obtained with hydrothermal method, PVD and CVD[9-12] etc., the difficulties in the controllable fabrication of uniform and large-area ReS_2 still greatly limit its scale production. Therefore, as an alternative to those traditional methods, recently bulk

ReS_2 on Al_2O_3 and 2-d ReS_2 on SiO_2/Si have been developed successfully with a ALD method by using $ReCl_5$ and H_2S as precursors,[13,14] which was a useful exploration for its manufacturing controllability.

Inspired by the rapid developments of ALD and low-dimensional doping strategy, a bimetallic co-chamber feeding ALD equipment was designed for MoS_2-ReS_2 heterojunction fabrication, by which a precise dose regulation was achieved for controllable Mo-to-Re ratio. In addition, the morphology and pattern of MoS_2-ReS_2 heterojunction could be regulated and simultaneously their electron transfer capacity, carrier mobility and photoelectric response could be improved, based on which ultrasensitive PEC platform can be integrated for miRNA-21 detection.

2. Experimental section

2.1 Reagents and materials

Indium-tin-oxide (ITO) slices (<5 ohm) were purchased from Shangzhuo Technology Co. Ltd (Luoyang, China). Rhenium pentachloride ($ReCl_5$, purity>99%) was purchased from China Rhenium Co. Ltd (Zhuzhou, China). Hydrogen sulfide (H_2S, 99.6%), Oxygen (O_2, 99.999%) and Nitrogen (N_2, 99.999%) were supplied by Nanjing Special Gas Co. Ltd (Nanjing, China). Molybdenum chloride ($MoCl_5$), hydrogen tetrachloroaurate trihydrate ($HAuCl_4 \cdot 3H_2O$), 6-mercaptohexanol (MCH), phosphate-buffer solution (PBS), streptavidin (SA), ascorbic acid (AA), potassium hexacyanoferrate-III ($K_3[Fe(CN)_6]$) and potassium hexacyanoferrate-II ($K_4[Fe(CN)_6]$) tri-hydrate were purchased from Sigma-Aldrich (Shanghai, China). The oligonucleotide sequences were provided by Sangon Biotech Co. Ltd (Shanghai,

China) and their sequences were as follows:

Probe SH-DNA: 5′-SH-GACCG TCA ACA TCA GTC TGA TAA GCT ACA CCA GGG ACG GTC-biotin-3′;

MiRNA-21: 5′-UAG CUU AUC AGA CUG AUG UUG A-3′;

Single-base mismatch miRNA: 5′-UAG CUU AUC AGA CUG AUG UUG C-3′;

MiRNA-155: 5′-UUA AUG CUA AUC GUG AUA GGG GU-3′;

MiRNA-182: 5′-UUU GGC AAU GGU AGA ACU CAC ACU-3’;

MiRNA-141: 5′-UAA CAC UGU CUG GUA AAG AUG G-3′.

Diethyl pyrocarbonate (DEPC) water was used for the preparation of all solutions to reduce the effect of RNase on the experimental results.

2.2 Characterization

Photoelectrochemical and electrochemical measurements were performed on an electrochemical workstation (CHI660E, China) with a conventional three-electrode system consisted of a saturated calomel electrode as reference electrode, a modified ITO (0.25 cm^2) as working electrode, and a platinum (Pt) wire as counter electrode. All the PEC measurements were operated at an applied potential of 0.1 V under a monochromatic light (1 W, 450 nm, 92 $mW \cdot cm^{-2}$) in the 0.1 M PBS buffer solution (pH=7.4) containing 0.1 M AA as the electron donor. The cyclic voltammetry (CV) were carried out in 5mmolL^{-1} $[Fe(CN)_6]^{3-/4-}$ containing 0.1 molL^{-1} potassium chloride (KCl) solution between −0.1V and 0.6 V. The impedance spectroscopy (EIS) measurements were implemented in the 0.1M PBS buffer solution (pH=7.4), containing 0.1 M KCl and 2.5 mM $[Fe(CN)_6]^{3-/4-}$ and all the obtained data

were processed by Zsimpwin. The effective surface was tested by chronocoulometry (CC) in 0.1 mM $K_3[Fe(CN)_6]$ with 1.0 M KCl, which was studied in our previous research.[15]

The composition, chemical bonds and the Mo/Re ratio of the surface layer of MoS_2-ReS_2 heterojunction films were analyzed by X-ray photoelectron spectroscopy (XPS, PHI Quantera II, Japan) with the Al Kα radiation line (1486.6 eV) and a power of 200 W. All the binding energies of the XPS spectra were calibrated using the C 1s (284.6 eV) of ambient hydrocarbons and peak fitting was completed using the XPSPEAK41 software. The element contents and the Mo-to-Re ratio were also measured by inductively coupled plasma optical emission spectrometer (ICP-OES, Spectroblue, Germany). The surface morphology of the film samples was examined by a scanning electron microscope (SEM, FEI Inspect F50, USA). The thickness of obtained films was identified by high-resolution transmission electron microscopy (HRTEM, JEM-2100, Japan). The composition and crystal structures of films were investigated by Raman spectroscopy (Raman, RAM-PRO-785E, USA), using a 532 nm laser. The microstructure of the film was observed by a transmission electron microscope (TEM, Titan80-300, USA). The substrate was treated with O_2 by a PCE-6 plasma cleaner.

2.3 Preparation of MoS_2, ReS_2 and MoS_2-ReS_2 heterojunctions

MoS_2, ReS_2 and MoS_2-ReS_2 heterojunctions were deposited in a homemade and multi-source controllable ALD setup operated under reduced nitrogen pressure. $ReCl_5$, $MoCl_5$ and H_2S were used as precursors for the deposition of MoS_2-ReS_2

heterojunctions thin films. In our previous researches, the ALD window of MoS_2 grown from $MoCl_5$ and H_2S had been determined as 370-490 ℃,[16] and 400 ℃ had been identified as the optimal temperature for ReS_2 thin films according to the crystallinity, coverage and the growth rate of the ReS_2 films deposited in different temperatures.[14] In the experiments, all the film samples were deposited in 400℃. The solid $ReCl_5$ and $MoCl_5$ precursors were kept at 110℃ and delivered into the reaction chamber with a N_2 carrier flow of 50 sccm.

The method for depositing MoS_2-ReS_2 heterojunctions by ALD was a combination of ReS_2 and MoS_2 ALD processes into a super-cycle. One super-cycle was composed of n_1 ReS_2 cycles and n_2 MoS_2 cycles and the number of n_1 and n_2 was determined by the total cycles of ReS_2 and MoS_2. Each ReS_2/MoS_2 cycle included $ReCl_5$/$MoCl_5$ pulsing (5 s), N_2 purging (55 s), H_2S pulsing (2 s) and N_2 purging (58 s). Moreover, when ReS_2 and MoS_2 cycle happened simultaneously in one super-cycle, $ReCl_5$ and $MoCl_5$ were injected into the reaction chamber together to obtain well-mixed MoS_2-ReS_2 heterojunctions. Furthermore, pure MoS_2 or pure ReS_2 films were prepared by the same ALD procedures without cycle for Re source or Mo source respectively. Before deposition, ITO substrates were cleaned by sonication in acetone, ethanol, and deionized water for 20min successively and dried under a N_2 flow, then treated with O_2 plasma for 60s.

2.4 Fabrication of PEC sensing platform

The fabrication of PEC miRNA sensing platform was illustrated in **Figure 6A**. MoS_2-ReS_2 heterojunctions were grown on the ITO substrates through a bimetallic

co-chamber feeding ALD setup. Au nanoparticles (AuNPs) were electrodeposited on the photoactive ITO electrodes to assemble probe thiolated DNA (SH-DNA). According to our previous research, by controlling the deposition potential at - 0.2V and deposition time at 300s, the AuNPs prepared by electrodeposition has good uniformity.[15] The obtained electrodes were noted as AuNPs/MoS_2-ReS_2/ITO. Then 20 μL probe DNA solution (1μM) was dripped onto AuNPs/MoS_2-ReS_2/ITO (named as SH-DNA/AuNPs/MoS_2-ReS_2/ITO) and the obtained electrodes were incubated for 6 h at room temperature in the dark environment. After the modified electrodes were washed with PBS buffer solution (pH=7.4) (to remove the unbound probe SH-DNA) and dried at room temperature, 20 μL MCH (10 μM) was dropped onto the surface of SH-DNA/AuNPs/ MoS_2-ReS_2/ITO (named as MCH/SH-DNA/AuNPs/MoS_2-ReS_2/ITO) for 60 min to fill unreacted AuNPs and block any nonspecific adsorption site. Similar to the above, the dried electrodes were rinsed with PBS buffer solution (pH=7.4) again. Then, 15 μL of miRNA-21 with certain concentration was trickled onto the surface of electrodes and incubated for 120 min at 37 ℃. Finally, 20 μL SA (15 μg/mL) was added to the modified electrodes for 30 min at room temperature (named as SA/miRNA/MCH/SH-DNA/AuNPs/MoS_2-ReS_2/ITO). Finally, the electrodes were washed and used as PEC anodes for photo-electrochemical measurements.

3. Results and Discussion

3.1 Controllable fabrication of MoS_2-ReS_2 heterojunctions

Pure ReS_2 films can be fabricated on ITO substrates in general ALD way using

$ReCl_5$ and H_2S as precursors at 400 ℃, whose structures can be confirmed by their Raman spectra. The SEM images of pure ReS_2 films obtained under 100, 150, 200, 250, 300 conventional ALD cycles (named the samples R-100, R-150, R-200, R-250, R-300 respectively) indicate their excellent coverage and consistency (**Figure 1A-E**). These SEM images show that the film gradually thickens and its aggregation state changes from nanoparticles to nanoflakes with the number of cycles increasing, partly because the rough ITO surface could be easy to induce vertical orientation of ReS_2.

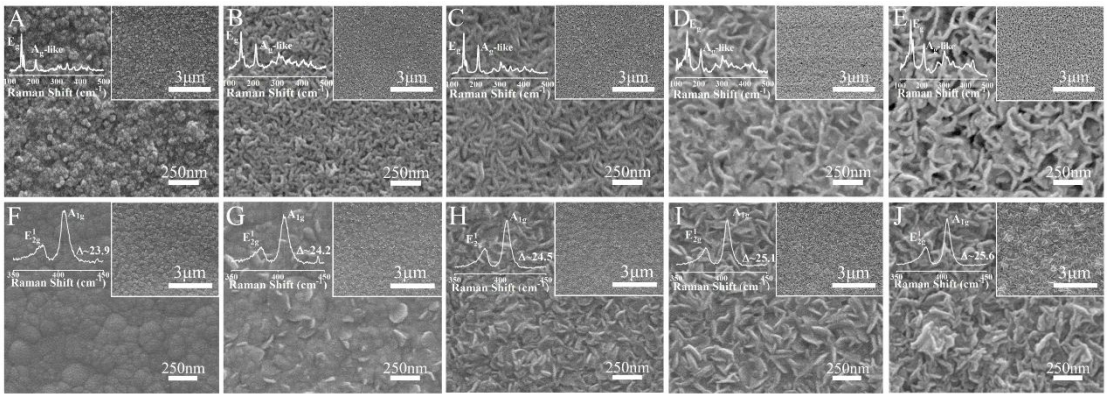

Figure 1. (A-E) SEM images of ReS_2 films grown on ITO substrates obtained under 100, 150, 200, 250 and 300 ALD cycles; (F-J) SEM images of MoS_2 films grown on ITO substrates obtained under 100, 150, 200, 250 and 300 ALD cycles. The insets in (A-J): the corresponding Raman spectra.

Furthermore, parallel orientation of ReS_2 is apt to form at rather a lower temperature and out of plane orientation prefers to forming at 400℃ and above[13]. In addition, the standing-up morphology with excellent coverage and consistency could provide more active sites and thus can support more AuNPs for improving the detection precision in the following work. From another perspective, the increase of electrical resistance can also indicate the accumulation of ReS_2, as shown in their electrochemical EIS results (**Figure S1**). Particularly, their photocurrents continue to

enlarge with ALD cycle increasing before the peak value at 200 ALD cycles. Generally, ReS_2 nanoflakes can exhibit a higher effective surface area (ESA) during their moderate accumulation, which provide more active sites to accelerate the electron transfer. However, with the increase of the number of ALD cycles, the excessive accumulation of ReS_2 blocks the electron transfer, resulting in the gradual reduction of photocurrents.

The same studies are carried out for pure MoS_2 prepared under 100, 150, 200, 250 and 300 general ALD cycles (named the samples M-100, M-150, M-200, M-250, M-300 respectively) using $MoCl_5$ and H_2S as precursors at 400℃ (**Figure 1F-J**). The distance of peak position between MoS_2 E^1_{2g} and A_{1g} modes changes from 23.9 to 25.6 with the ALD cycles increasing, which indicates the aggregation of MoS_2.[17,18]

Table 1. The detailed fabrication information of MoS_2-ReS_2 heterojunctions

Sample ID	ALD manufacturing process for each sample		Mo-to-Re feed ratio (R_f)	Mo-to-Re real ratio (R_r)
	one super-cycle	Repeat time		
RM-0	1 **RS** only	200	0	0
RM-1	9 **RS** followed by 1 **RMS**	20	20/200 (10%)	14.8% (±3.1)
RM-2	4 **RS** followed by 1 **RMS**	40	40/200 (20%)	22.6% (±4.5)
RM-3	1 **RS** followed by 1 **RMS**	100	100/200 (50%)	40.3% (±4.4)
RM-4	1 **RS** followed by 3 **RMS**	50	150/200 (75%)	57.8% (±9.0)
RM-5	1 **RMS** only	200	200/200 (100%)	76.5% (±18.5)
RS: one $ReCl_5$ pulse followed by one H_2S pulse; **RMS**: one $ReCl_5$ pulse and one $MoCl_5$ pulse followed by one H_2S pulse.				

According to the manufacturing process for the best photocurrent response of ReS_2 (200 ALD cycles), MoS_2-ReS_2 heterojunctions have been fabricated by a precise dose regulation strategy in a bimetallic co-chamber feeding ALD (**Table 1, Figure 2A**)[19],

which designs pulsing $ReCl_5$ and $MoCl_5$ precursors alternately into the same ALD reaction chamber in one "super cycle" (**Table 1** or Experimental section). At the same time, the purging time before dosing precursors remains as long as possible to guarantee the purity of reaction and the controllability of film.

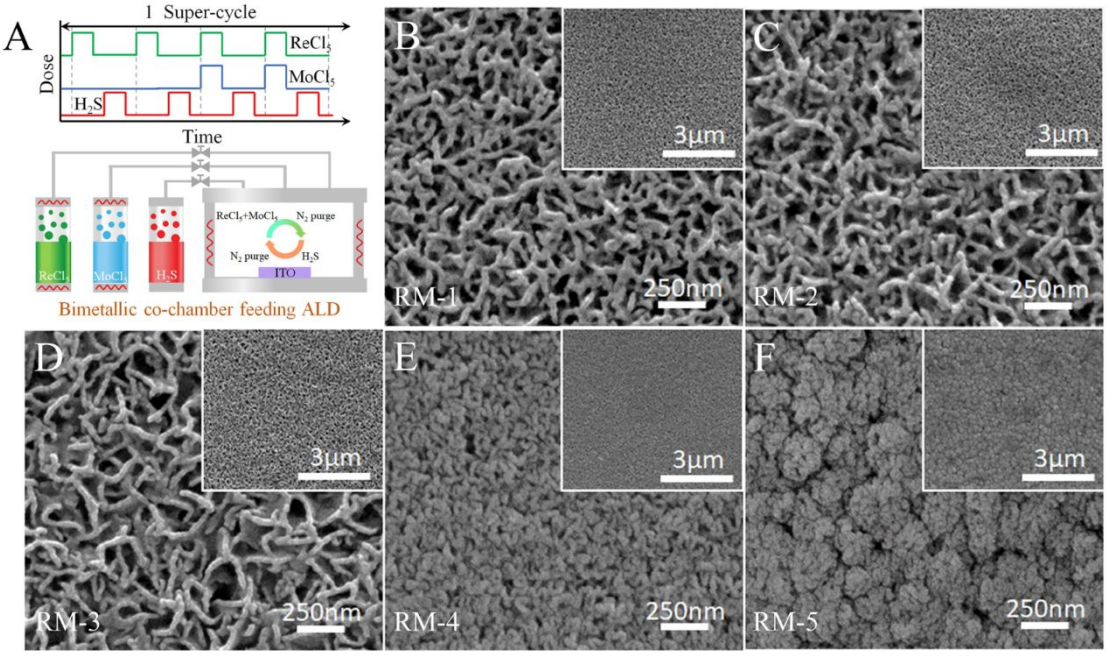

Figure 2. (A) Schematic images of a bimetallic co-chamber feeding ALD setup and the co-dosing ALD procedure for the preparation of MoS_2-ReS_2 heterojunctions. (B-F) SEM images of RM-1, RM-2, RM-3, RM-4, RM-5.

As shown in **Figure 2B** to **Figure 2F**, when the feed Re-to-Mo ratio (R_f=N_{ReS2}/ N_{MoS2}, N_{MoS2} or N_{ReS2} represent the corresponding pulse quantity of $ReCl_5$ or $MoCl_5$ in one "super cycle") is less than 50% (for RM-1 and RM-2), the heterojunction samples show intense vertical trends and plate-like crystals are orientated more randomly against substrates, which indicates that the growth tendency of ReS_2 is barely affected by doping a small amount of Mo, but promoting the vertical direction to some extent. However, the aggregation state of RM-4 (R_f=75%) changes from plate-like morphology into flake-like morphology, and agglomerate more and more

when R_f =100% (RM-5).

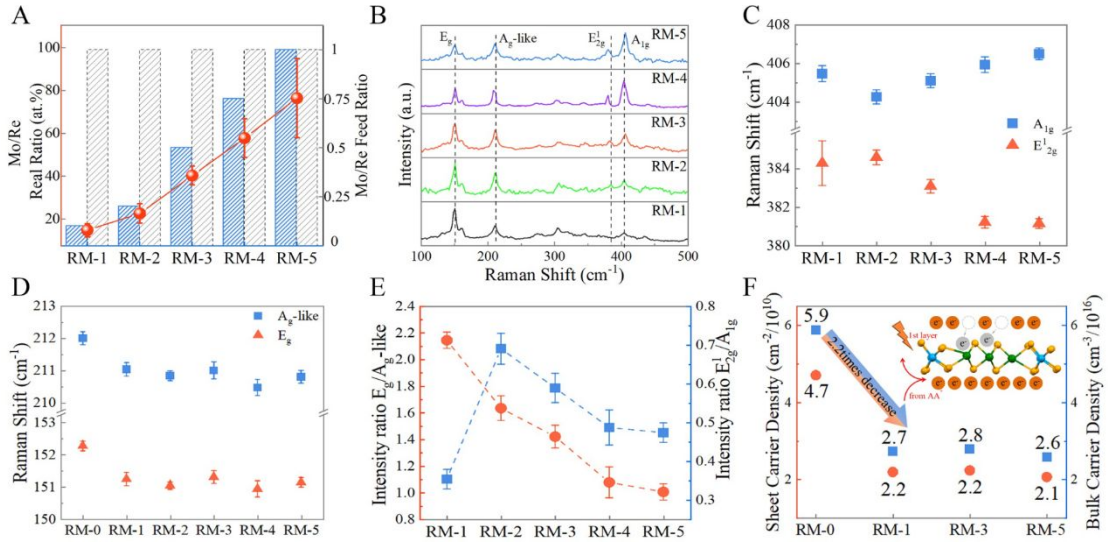

Figure 3. (A) The variation of the Mo-to-Re ratio for MoS_2-ReS_2 heterojunctions; (B) Raman spectra of different MoS_2-ReS_2 heterojunctions samples; (C) Evolution of peak positions of E^1_{2g} and A_{1g} modes in MoS_2; (D) Evolution of peak positions of E_g and A_g-like modes in ReS_2; (E) Evolution of E^1_{2g}/A_{1g} in MoS_2 and E_g/A_g-like in ReS_2 intensity ratio for different MoS_2-ReS_2 heterojunctions samples; (F) The carrier density of different MoS_2-ReS_2 heterojunctions samples tested in Hall measurement and inset shows the schematic of the electron-trapping effect caused by MoS_2-ReS_2 heterojunctions.

The real Mo-to-Re ratio (R_r) of these samples has been measured by ICP-OES (**Table 1**, **Figure 3A**), which are consistent with the corresponding XPS results (**Table S1**). R_r exhibits a nonlinear increasing trends with Mo increasing, as follows: 10% of R_f corresponds to 11.7%~17.9% of R_r; 20% of R_f accounts for 18.1%~27.1% of R_r; Then R_r can be controlled and stabilized at about 40.3% even when R_f=50%; however, 100% of R_f only results in about 76.5% of R_r. When R_f is under 50%, R_r is close to R_f and with less fluctuation. When R_f further increases, the gap between R_r and R_f is growing and the fluctuation range of R_r is also increasing, which can be attributed to the self-limited reaction of ALD and the discrepancy of adsorption capacity caused by temperature. Firstly, for the self-limited reaction of ALD in each

super ALD cycle, the chemisorption of precursors is limited and regular, while the growth active sites are generally at the edge of film formed in the previous pulse (**Figure S2**).[20] When R_f is under 50%, the adsorption site is sufficient and $MoCl_5$ and $ReCl_5$ are in the state of free adsorption, so the R_r is close to R_f and fluctuates less. In addition, when the mixed precursor is more than enough, these limited sites are filled up rapidly, which increases the randomness of the chemisorption and film growth. Meanwhile, 400 ℃ is not the optimal temperature for the chemisorption of $MoCl_5$ (its optimal temperature is 460 ℃), although it is still in the ALD growth window for MoS_2. [16] When R_f is over 50%, the metal precursor is over saturated and $MoCl_5$ and $ReCl_5$ are in a state of competitive and random adsorption. Under this condition, the adsorption capacity of $MoCl_5$ is weaker than that of $ReCl_5$, so the gap between R_r and R_f is growing and the fluctuation range is also increasing. Furthermore, excessive dense nucleation points can result in smaller grains which are corresponding to the morphology changes.

Also, Raman spectra can reflect the formation of the heterojunctions (**Figure 3B**). ReS_2 has more than 10 vibrational modes due to its anisotropic structure, thus it gives the characteristic peaks at 150 cm^{-1} (E_g) and 210 cm^{-1} (A_g-like) and other peaks from 250 cm^{-1} to 550 cm^{-1}.[20,21] But, the obvious peak at 404 cm^{-1} in the spectrum for RM-1 cannot be regarded as the direct evidence of the existence of MoS_2. For the samples with the increase of Mo pulsing numbers (RM-2, 3, 4, 5), the increasing intensity of the peaks around 385 cm^{-1} and 404 cm^{-1} (E^1_{2g} and A_{1g} for MoS_2) displays solid evidence for the formation of MoS_2,[17,18] while the intensity of ReS_2-related peaks

decreases at the same time. The evolution of peak position of E^1_{2g} and A_{1g} modes in MoS_2 indicates that the peak position of MoS_2 in-plane modes (E^1_{2g}) obviously soften (red shift) by 3 cm^{-1} (**Figure 3C**), resulted from the strain effect from the coupling of the in-plane MoS_2 and ReS_2.[22,23,24] Another interesting phenomenon to note is that MoS_2 out-plane modes (A_{1g}) stiffen (blue shift) slightly. MoS_2 A_{1g} mode is insensitive with the strain effect,[25,26] which can be ascribed to the stacking of MoS_2-ReS_2 heterojunctions. In the meantime, the distance between E^1_{2g}-related and A_{1g}-related peaks increasing from 19.8 cm^{-1} to 25.2 cm^{-1} also indicates the enlarged thickness of MoS_2 in the heterojunctions. Similarly, compared with pure ReS_2, the ReS_2-related peak position values of RM-1 to RM-5 soften by 1 cm^{-1} (**Figure 3D**), which could be affected by the electron–phonon coupling in TMDs.[8] The intensity ratio of dual modes also reflects the formation of MoS_2-ReS_2 heterojunctions.[22,23,27] A sustained drop in the intensity ratio of MoS_2 E^1_{2g}/A_{1g} and ReS_2 E_g/A_g-like (except the MoS_2 E^1_{2g}/A_{1g} intensity ratio of RM-1 due to its unconspicuous MoS_2 modes) can be confirmed (**Figure 3E**), which is consistent with the coupling effects of MoS_2 and ReS_2.[22,23] A_{1g} mode of MoS_2 shows a strong negative charge doping dependence, and E^1_{2g} mode is insensitive to charge doping, so the decrease of E^1_{2g}/A_{1g} in MoS_2 corresponds to the alleviation of the negative charge doping propensity of MoS_2, indicating the electron transfer from MoS_2 to ReS_2 and possible electron trapping effect of the ReS_2.[27,28] When electrons transfer from MoS_2 to ReS_2, the energy band will be bent on the interface of heterojunctions and a potential barrier can be formed at the electron donor (MoS_2). In the meantime, a potential well can be formed at the

electron acceptor (ReS_2), in which electrons are gathered and constrained. As illustrated in **Figure 3F**, the carrier density of MoS_2-ReS_2 heterojunctions decreases 2.2 times than that of pure ReS_2, resulted from the electron-trapping effect in MoS_2-ReS_2 heterojunction.[27,28] At the same time, the red shift of Raman peaks could be attributed to the less carrier interacting with incoming photons and leading to the shift to lower frequency,[8] while the electron trapping effect caused by charge doping is limited. Referring to previous research results, when 5% of Re atoms dopes with MoS_2, charge doping effect is saturated,[27] thus the carrier density of RM-1 to RM-5 does not decrease continuously.

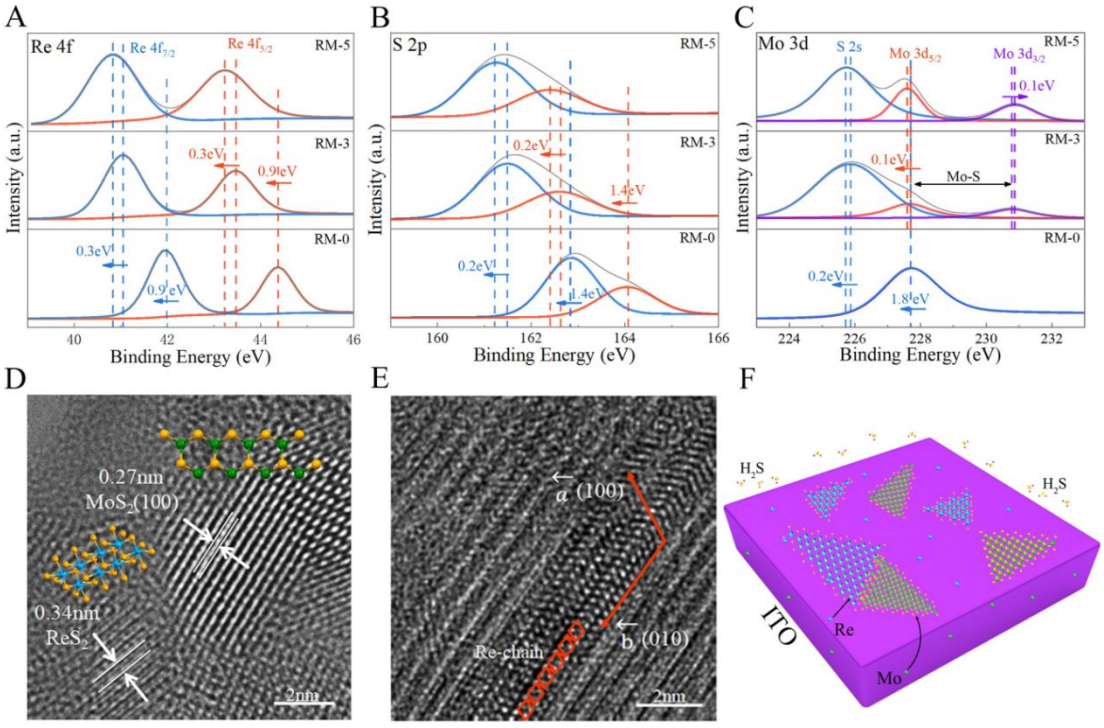

Figure 4. Re 4f (A), S 2p (B), Mo 3d (C) XPS spectra of ReS_2 film and RM-3, RM-5. HR-TEM of MoS_2-ReS_2 heterojunctions (D) and ReS_2 films (E). The schematic (F) for the MoS_2-ReS_2 heterojunctions prepared by bimetallic co-chamber feeding ALD.

Furthermore, the Re 4f-related XPS peaks for pure ReS_2 at 42.0 eV and 44.4 eV correspond to Re $4f_{7/2}$ and Re $4f_{5/2}$ binding energies of Re^{4+}, which indicate no ReO_3

in the film (**Figure 4A**). When Mo pulse is increasing, obvious blue shifts (0.9 eV for RM-3 and 1.1 eV for RM-5) appear in two Re 4f-related peaks. The full width at half maximum intensity of the two peaks slightly increases, owing to the increasing complexity of elements. What is more, the same can be observed in the S 2p-related peaks: two peaks shift toward lower energy direction (1.4 eV for RM-3 and 1.6 eV for RM-5) compared to that for ReS_2. In Mo 3d-related curve for pure ReS_2, the only peak (227.7 eV) between 224.0 eV and 232.0 eV is attributed to Re-S bonds. After Mo incorporation, S 2s-related peak shifts to blue direction by 1.8 eV, and the appeared Mo^{4+} 3d-related peak indicates the formation of Mo-S bonds.[8] In addition, with the sustained increase of Mo element, Mo^{4+} 3d-related peak enhances, and S 2s-related peak shifts to the low energy direction by 0.2 eV. The down shift of Re-related and S-related peaks can be attributed to the charge transfer from MoS_2 to ReS_2.[22,24] The down shift of ReS_2 corresponds to a negative net charge on the ReS_2, but Mo 3d-related peak does not show an up-shift, corresponding to a positive net charge on MoS_2, which is caused by the formation of 1T-MoS_2. The Mo 3d-related peaks of 1T-MoS_2 will be about 1eV lower than those of 2H-MoS_2.[25,26] XRD spectrum as the further evidence for the formation of 1T-MoS_2 (**Figure S3**) illustrates the significant peak at 14.3°, which can be attributed to both ReS_2 and MoS_2 because of the most significant peaks of 2H-MoS_2 (14.1°) and ReS_2 (14.5°) all around 14.3°. Furthermore, the unique peak at 7.3° is the most important evidence for the formation of 1T-MoS_2. In addition, the peak at 22.4° is attributed to quartz glass sample holder. The transformation from 2H-MoS_2 to 1T-MoS_2 may result from the stress that is

caused by the coupling effect of 2H-MoS_2 and distorted 1T-ReS_2, which also leads to the metalloid transition of the system.[29]

The combination manner of MoS_2 with ReS_2 can be observed by EDS elemental mappings of RM-3 (**Figure S4**), which indicates that Re and Mo elements are evenly distributed on the ITO surface, confirming that RM-3 prepared by the bimetallic co-chamber feeding ALD is composed of MoS_2 and ReS_2. The atomic percentage of Re, Mo and S are 30.9%, 10.1% and 59%, respectively. The ratio of Mo/Re is in accordance with the results of ICP and XPS. In addition, the ratio of (Mo+Re)/S is greater than 1/2, indicating that MoS_2 and ReS_2 prepared by ALD has S defect which is line with our previous work.[14] Most intuitively, HRTEM image (**Figure 4D**) demonstrates directly the formation of the in-plane heterojunction between local ReS_2 region and local MoS_2 region. Generally, the metal precursors are pulsed into the same ALD chamber simultaneously, while of $ReCl_5$ and $MoCl_5$ may not mix completely and homogeneously. Additionally, the active sites for the cyclical chemical reaction existed in the surface and edge of the existed film; and the chemical adsorption is more likely to occur between the same kinds of materials, which can be confirmed by the existed Re atomic chains (**Figure 4E**). In addition, **Figure 4F** shows the strategy for the MoS_2-ReS_2 heterojunctions by bimetallic co-chamber feeding ALD.

3.2 Performance optimization

ReS_2 films obtained by ALD method possess good photoelectric properties, which benefits from their direct band gap and high films quality (**Figure 5A**). Moreover,

MoS_2-ReS_2 heterojunction samples display a significant improvement in photoelectric properties. Compared with MoS_2 and ReS_2, especially RM-3 shows the most excellent photocurrent response (172 μA), which is almost 7 times more than that of pure ReS_2 and 59 times more than that of pure MoS_2.

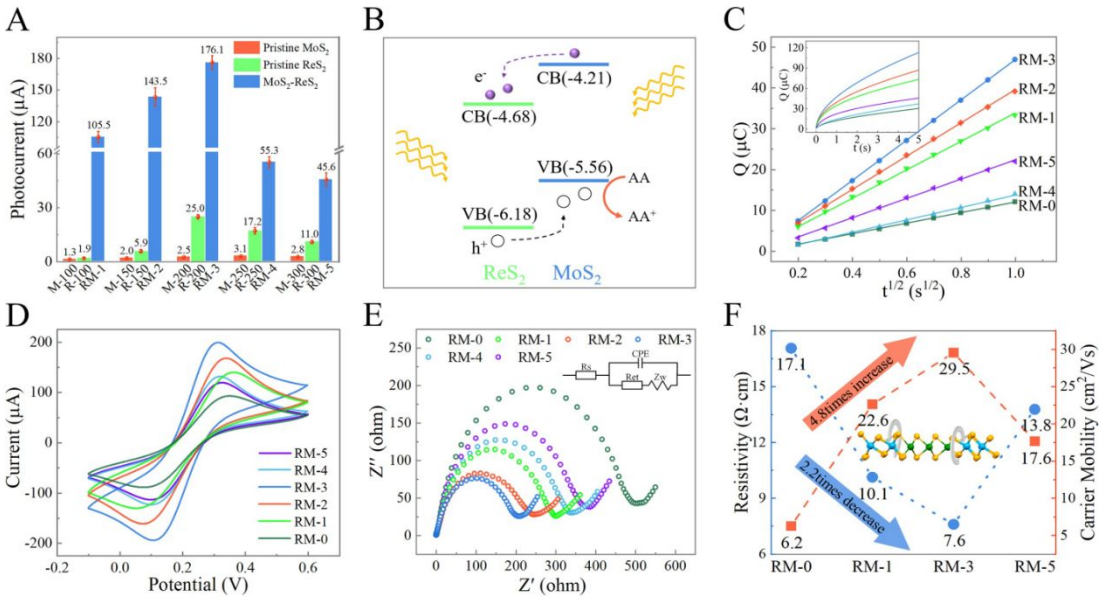

Figure 5. (A) The photocurrent response of pure MoS_2, ReS_2 with different ALD cycles and different heterojunction sample; (B) Schematic diagram of the band structure and charge transfer of MoS_2-ReS_2 heterojunctions; (C) The effective surface area, (D) CV and (E) EIS of pure MoS_2, ReS_2 and different heterojunction samples; (F) The resistivity and carrier mobility of different heterojunction samples tested in Hall measurement. Inset in (E): The schematic of equivalent circuit was consisted of solution resistance (Rs), electron-transfer resistance (Ret), constant-phase element (CPE), and Warburg impedance (Zw); Inset in (F): The metallic system caused by the stress at lattice junction.

As shown in the illustrated image of the band structure and charge transfer for MoS_2-ReS_2 heterojunctions (**Figure 5B**), the conduction band minimum (CBM) , valence band maximum (VBM) and work function of MoS_2 and ReS_2 are reported to be 4.21, 5.56, 4.5 eV and 4.68, 6.18, 5.1 eV.[30,31] Due to the higher work function of ReS_2, the charge is more likely to transfer from MoS_2 to ReS_2,[22,32] which is in line with the results of XPS and Raman spectra. Moreover, the VBM of MoS_2 lies in the

band gap of ReS_2. Thus MoS_2-ReS_2 heterojunction is a kind of type-Ⅱ heterojunctions,[33] which is advantageous to prevent the recombination of hole-electron pairs with long-lived interlayer excitons to improve the performance in photocurrent response. At the same time, the lattice difference between MoS_2 and ReS_2 would result in lattice mismatch, which would prevent the recombination of hole electron pairs to some extent to enhance photoelectric capability.

Meanwhile, the ESA of pure ReS_2 films is 0.32 cm^2 (**Figure 5C**), which is slightly larger than that of ITO (0.25 cm^2). The ESA of RM-1, RM-2, RM-3, RM-4 and RM-5 are 1.15, 1.31, 1.64, 0.50, 0.78 cm^2 respectively, which match their micromorphology well (**Figure 2B** to **Figure 2F**). Obviously, the ESA value is enlarged with Mo increasing and reaches the maximum at R_f=50%, while excessive Mo atoms will result in a sharp decrease in grain and ESA. Higher ESA can provide more active sites to carry gold nanoparticles to improve the detection accuracy.[15]

The CV (**Figure 5D**) and EIS (**Figure 5E**) are used to evaluate the ability of electron transfer on the modified electrode interface. Similar to the performance in the photocurrent and ESA, the peak currents of MoS_2-ReS_2 heterojunctions are significantly higher than pure ReS_2 in CV plot. In addition, RM-3 shows the highest peak value, indicating the best electron transfer capability. The electron-transfer resistance (Ret) values calculated from the equivalent circuit for MoS_2-ReS_2 heterojunctions are quite less than that for pure ReS_2 (111.7 Ω). The minimum value (44.7 Ω) corresponds to RM-3 (R_f=50%), and Ret values for RM-1, RM-2, RM-4 and RM-5 are 54.0 Ω, 63.6 Ω, 82.4 Ω and 99.7 Ω respectively. Obviously, the

heterojunction structure decreases Ret value and facilitates electron transfer between the surface of material and solution, thus improve the photoelectric properties. The Hall Effect Measurements also indicate that heterojunction structure can result in quite a lower resistance and higher electron mobility, which further verify the effect of Mo atoms in carrier mobility and resistivity (**Figure 5F**). The system becomes metallic (lower resistance and higher carrier mobility), which could result from the stress effect in heterojunction,[29] and is in line with the results of peak position shift in XPS spectra.

3.3 Ultrasensitive miRNA-21 detection based on MoS_2-ReS_2 heterojunctions

RM-3 which exhibits an excellent photoelectric conversion capacity (172 μA) is used in the ultrasensitive nanodevice integration for miRNA-21 detection (**Figure 6A**). AuNPs are deposited on MoS_2-ReS_2 heterojunction/ITO to immobilize probe DNA by Au-S bond with electrodeposition method and AuNPs are fixed on the surface modified electrodes by van der waals force. The deposition of AuNPs on electrode surface results in a slightly decrease in photocurrent (159 μA, **Figure 6B**), which may be ascribed to three factors: the first is the easy recombination of photo-generated electrons and holes in system by AuNPs with captured AA, the second is the vibration relaxation resulted from the plasmin resonance effect at the surfaceof AuNPs; the last is the repulsion between negatively charged AuNPs and the negatively charged AA. +0.1 V voltage is applied to the electrodes, which could ensure that the electron donor in the solution could reaches the electrode surface smoothly and immunity from repulsion forces between AuNPs and AA. AuNPs

possess good conductivity, whose accumulation can result in a sharp decrease in the electric resistance. Under the coupling effects of AuNPs and MoS_2-ReS_2 heterojunctions, the photocurrent decrease slightly.

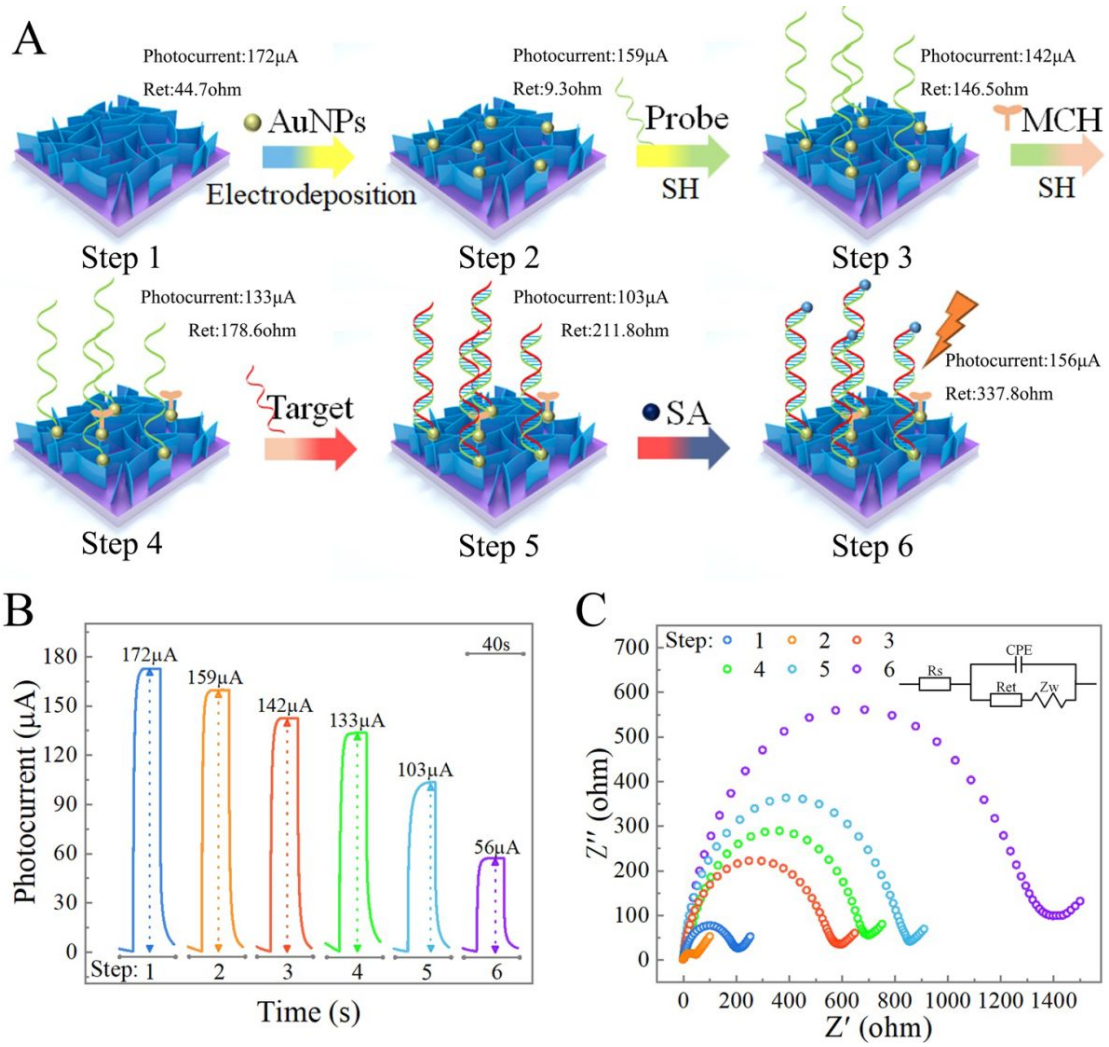

Figure 6. (A) Illustration of the proposed PEC biosensor for miRNA-21 Detection. (B, C) The photocurrent response and EIS images of different electrodes during the built of sensing platform, in which MoS_2-ReS_2/ITO, AuNPs/MoS_2-ReS_2/ITO, SH-DNA/AuNPs/MoS_2-ReS_2/ITO, MCH/SH-DNA/AuNPs/MoS_2-ReS_2/ITO, miRNA/MCH/SH-DNA/AuNPs/MoS_2-ReS_2/ITO, SA/miRNA/MCH/SH-DNA/AuNPs/MoS_2-ReS_2/ITO are step (1-6) respectively.

In our work, the photocurrent continues to drop as probe DNA (142 μA), MCH (133 μA), target RNA (103 μA), and SA (56 μA) being added in turn and the Ret value also increases gradually (**Figure 6C**). The negatively charged probe DNA and

target RNA will inhibit the electron transfer, and the short alkanethiol of MCH will block electron transfer from solution to electrodes. In addition, the immobilization of SA with miRNA and AuNPs increases the steric hindrance from AA to the surface of electrodes.

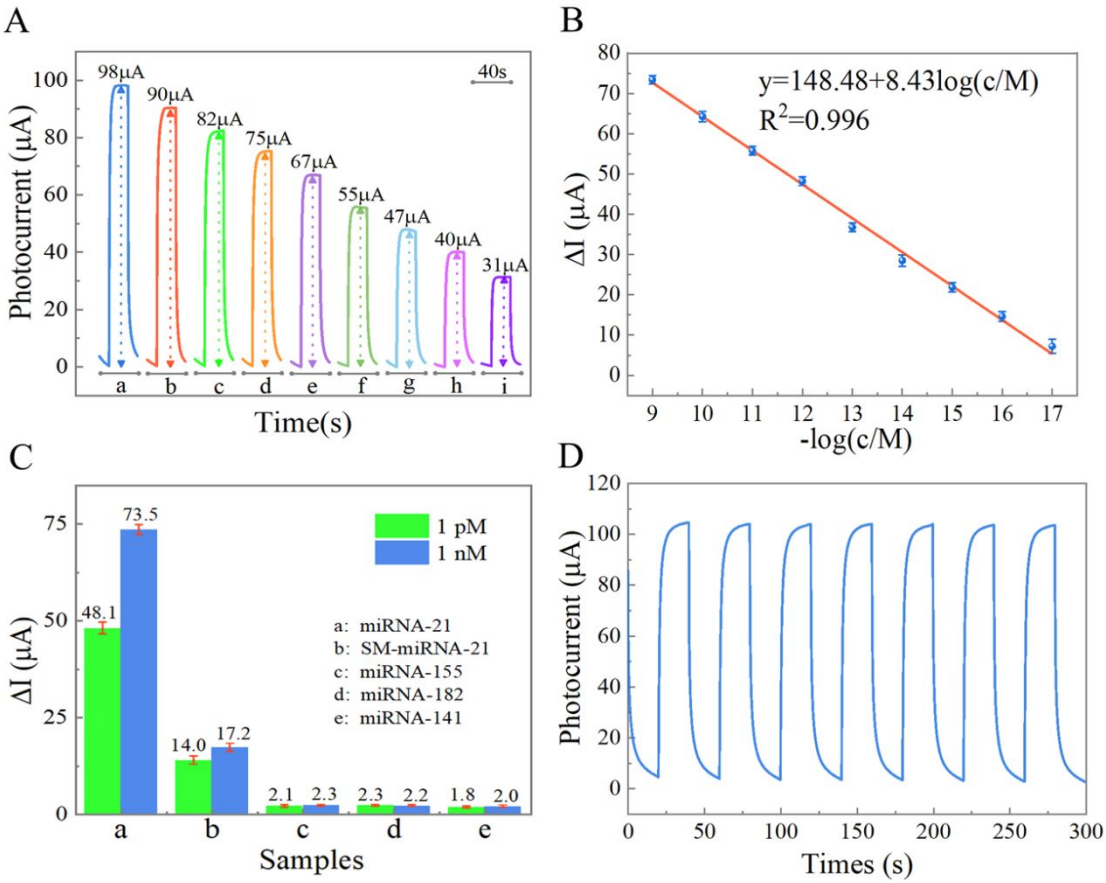

Figure 7. (A) Photocurrent response to different concentrations of miRNA-21 from (a)-(i): 10 aM, 100 aM, 1 fM, 10 fM, 100 fM, 1 pM, 10 pM, 100 pM, 1 nM. (B) The calibration curve of the photocurrent versus logarithm value of miRNA-21 concentration. Error bars = standard deviations (n =5). (C) The selectivity of the sensing platform hybridized to 1 pM and 1 nM miRNA-21 (a), single-base mismatch miRNA-21 (b), miRNA-155 (c), miRNA-182 (d) and miRNA-141 (e). (D) The stability of the photocurrent response in 0.1 M PBS solution containing 0.1 M AA with light on and off.

In addition, the binding degree of probe RNA and miRNA-21 is affected by the incubation temperature and hybridization time, thus the above parameters are further optimized in **Figure S5**. The photocurrent continues to drop until the hybridization

time extends to 2 h, indicating it is enough for fully hybridization of target and probe. At the same time, 37 °C is the optimized incubation temperature, which is near the normal human body temperature. Therefore, 2 h and 37 °C are employed as the time and temperature for subsequent experiments.

Based on the above platform, miRNA-21 can be detected ultrasensitively from 10 aM to 1 nM (**Figure 7A**). With miRNA-21 concentration increasing, the photocurrent intensity decreases because of the gradual increased steric hindrance caused by more miRNA being blocked the diffusion of AA. From the linear relationship between ΔI and the logarithm for the concentration of miRNA-21 (**Figure 7B**), $\Delta I = 148.48 + 8.43\log(c/M)$ can be obtained with the correlation coefficient R^2=0.996 and the detection limit of 2.8 aM (S/N=3). The detection specificity is then compared by the photocurrent change (ΔI) with single-base mismatch miRNA and noncomplementary miRNA detected at 1.0 pM and 1.0 nM respectively (**Figure 7C**). The ΔI of proposed biosensor is almost 48.1 μA in the presence of target miRNA-21, which is almost 3.1 folds, 23 folds, 21 folds and 27 folds than the addition of single-base mismatched miRNA-21, three-base mismatched miRNA-155, miRNA-182, and miRNA-141. With the miRNA concentration increasing to 1 nM, the value of ΔI for miRNA-21 increase significantly, and the value of ΔI for SM-miRNA-21 increased slightly, while that of noncomplementary miRNA remains almost unchanged, indicating that the proposed biosensor possesses a high selectivity for the determination of miRNA-21. Moreover, the immobilization of SA with miRNA and AuNPs improved the specificity of detection through "signal-off" effect.

The stability of photocurrent responses is tested with signal on and off for 7 times during 300 s. No significant change of photocurrent change is observed together with the RSD value of 0.2%, which indicate an excellent stability. These results together with other results reported recently for miRNA-21 detection are listed in the **Table 2**.

Table 2. Comparisons of biosensing results for miRNA-21.

SN	Materials	Analytical Methods	Linear range(M)	Detection limit(M)	References
1	IS-AgNPs@Si	SERS	1×10^{-14} ~ 1×10^{-6}	3.5×10^{-15}	34
2	SiNWAs / Au	SERS	1×10^{-16} ~ 1×10^{-9}	3.4×10^{-16}	35
3	PEI-Ru(II)	ECL	5×10^{-16} ~ 1×10^{-11}	1.7×10^{-16}	36
4	g-C3N4 @AuNPs	ECL	1×10^{-15} ~ 1×10^{-11}	3.0×10^{-16}	37
5	MoS_2 microcubes	DPV	1×10^{-16} ~ 1×10^{-11}	8.6×10^{-17}	38
6	AuNPs@MoS_2	DPV	1×10^{-14} ~ 1×10^{-9}	7.8×10^{-16}	39
7	CeO_2-Au@GOx	DPV	1×10^{-15} ~ 1×10^{-11}	4.3×10^{-16}	40
8	TiO_2-α-Fe_2O_3	PEC	1×10^{-15} ~ 1×10^{-11}	3.2×10^{-16}	41
9	Bi_2WO_6@Bi_2S_3	PEC	1×10^{-15} ~ 1×10^{-9}	2.6×10^{-16}	42
*	**MoS_2-ReS_2**	**PEC**	**1×10^{-17} ~ 1×10^{-9}**	**2.8×10^{-18}**	**This work**

On the other hand, the long-term stability is undoubtedly very important for a biosensor. The modified electrodes were kept in darkness at 4 ℃ for 10 days and it maintains 89.6% of the initial photocurrent intensity for 1.0 pM miRNA-21 (**Figure S6**). In addition, the practicability of the proposed platform in real sample is evaluated by standard addition method. A group of real samples are prepared by adding four different concentration of miRNA-21 into human serum. As listed in the **Table S2**, the recoveries are 103.5%, 97.6%, 95.1% and 99.4% for human serum samples containing 1 nM, 10 pM, 100 fM, 1 fM miRNA-21 respectively and the RSD was less than 5%, indicating that the fabricated electrodes show good performance in real biological samples. Moreover, in order to test the sensor platform reproducibility, ten independent sensors are constructed on one day for the parallel detecting of target miRNA at 0.01 fM, 0.01 pM, and 0.01 nM, respectively, which show very small

result fluctuations with all of the RSD lower than 2.3% (**Figure S7**).

4. Conclusion

In summary, the out-plane oriented ReS_2 nanoflakes obtained under 200 ALD cycles possessed a better photocurrent response, based on which MoS_2-ReS_2 heterojunctions were fabricated by a bimetallic co-chamber feeding ALD. By the precise dose regulation, Mo-to-Re ratio in heterojunction samples could be effectively controlled, and the sample obtained under 100 "super cycles" (the "super cycle" for this sample containing 1 $ReCl_5$ pulse, 1 H_2S pulse, 1 $ReCl_5$ pulse and 1 $MoCl_5$ pulse, 1 H_2S pulse in turn, R_r=57.9%) exhibited the best photocurrent response. The incorporation of Mo improved the electron transfer capacity and carrier mobility. Finally, a "signal off" PEC detection platform was fabricated based the optimized heterojunction sample for miRNA-21 detection, which offered a linear detection window from 10 aM to 1 nM with a low detection limit of 2.8 aM.

Acknowledgments

This work is financially supported by the National Natural Science Foundation of China (51822501, 51805248), the Natural Science Foundation of Jiangsu Province (BK20170023, BK20181274), the grants from Top 6 High-Level Talents Program of Jiangsu Province (2017-GDZB-006, Class A), the International Foundation for Science, Stockholm, Sweden, the Organization for the Prohibition of Chemical Weapons, The Hague, Netherlands, through a grant to Lei Liu (F/4736-2).

Supporting Information

The EIS data of pristine ReS_2 grown under different ALD cycles; the growth

mechanism illustration of bimetallic co-chamber feeding ALD; detailed characterizations (EDS mapping, XRD) of MoS_2-ReS_2 heterojunction; parameter optimization of incubation temperature and hybridization time; the long-term stability and reproducibility of proposed biosensor; the elemental compositions of MoS_2-ReS_2 heterojunctions analyzed by XPS; the feasibility of proposed biosensor in human serum.

References

(1) Zhang, Q.; Fu, L. Novel Insights and Perspectives into Weakly Coupled ReS_2 toward Emerging Applications. *Chem* **2019**, *5*, 505-525.

(2) Rahman, M.; Davey, K.; Qiao, S. Advent of 2D Rhenium Disulfide (ReS_2): Fundamentals to Applications. *Adv. Funct. Mater.* **2017**, *27*, 1606129-1606150.

(3) Gutiérrez-Lezama, I.; Reddy, B. A.; Ubrig, N.; Morpurgo, A. F. Electroluminescence from indirect band gap semiconductor ReS_2. *2D Mater.* **2016**, *3*, 45016-45024.

(4) Zang, Y.; Lei, J.; Ju, H. Principles and applications of photoelectrochemical sensing strategies based on biofunctionalized nanostructures. *Biosens. Bioelectron.* **2017**, *96*, 8-16.

(5) Liu, E.; Long, M.; Zeng, J.; Luo, W.; Wang, Y.; Pan, Y.; Zhou, W.; Wang, B.; Hu, W.; Ni, Z.et al. High Responsivity Phototransistors Based on Few-Layer ReS_2 for Weak Signal Detection. *Adv. Funct. Mater.* **2016**, *26*, 1938-1944.

(6) Zhang, K.; Bersch, B. M.; Joshi, J.; Addou, R.; Cormier, C. R.; Zhang, C.; Xu, K.; Briggs, N. C.; Wang, K.; Subramanian, S.et al. Tuning the Electronic and Photonic

Properties of Monolayer MoS_2 via In Situ Rhenium Substitutional Doping. *Adv. Funct. Mater.* **2018**, *28*, 1706950-1706957.

(7) Suh, J.; Park, T.; Lin, D.; Fu, D.; Park, J.; Jung, H. J.; Chen, Y.; Ko, C.; Jang, C.; Sun, Y.et al. Doping against the Native Propensity of MoS_2: Degenerate Hole Doping by Cation Substitution. *Nano Lett.* **2014**, *14*, 6976-6982.

(8) Qin, J.; Shao, W.; Xu, C.; Li, Y.; Ren, D.; Song, X.; Zhen, L. Chemical Vapor Deposition Growth of Degenerate p-Type Mo-Doped ReS_2 Films and Their Homojunction. *ACS Appl. Mater. Inter.* **2017**, *9*, 15583-15591.

(9) Ye, L.; Ma, Z.; Deng, Y.; Ye, Y.; Li, W.; Kou, M.; Xie, H.; Zhikun, X.; Zhou, Y.; Xia, D.et al. Robust and efficient photocatalytic hydrogen generation of ReS_2/CdS and mechanistic study by on-line mass spectrometry and in situ infrared spectroscopy. *Appl. Catal. B-Environ.* **2019**, *257*, 117897-117906.

(10) Qi, F.; Chen, Y.; Zheng, B.; Zhou, J.; Wang, X.; Li, P.; Zhang, W. Facile growth of large-area and high-quality few-layer ReS_2 by physical vapour deposition. *Mater. Lett.* **2016**, *184*, 324-327.

(11) An, Q.; Liu, Y.; Jiang, R.; Meng, X. Chemical vapor deposition growth of ReS_2 nanowires for high-performance nanostructured photodetector. *Nanoscale* **2018**, *10*, 14976-14983.

(12) Al-Dulaimi, N.; Lewis, D. J.; Zhong, X. L.; Azad Malik, M.; O'Brien, P. Chemical vapour deposition of rhenium disulfide and rhenium-doped molybdenum disulfide thin films using single-source precursors. *J. Mater. Chem. C* **2016**, *4*, 2312-2318.

(13) Hämäläinen, J.; Mattinen, M.; Mizohata, K.; Meinander, K.; Vehkamäki, M.; Räisänen, J.; Ritala, M.; Leskelä, M. Atomic Layer Deposition of Rhenium Disulfide. *Adv. Mater.* **2018**, *30*, 1703622-1703628.

(14) Lv, J.; Liu, L. Direct fabrication of two-dimensional ReS_2 on SiO_2/Si substrate by a wide-temperature-range atomic layer deposition. *Nanotechnology* **2020**, *31*, 55602-55612.

(15) Liu, L.; Zhu, S.; Wei, Y.; Liu, X.; Jiao, S.; Yang, J. Ultrasensitive detection of miRNA-155 based on controlled fabrication of AuNPs@MoS_2 nanostructures by atomic layer deposition. *Biosens. Bioelectron.* **2019**, *144*, 111660-111667. (16) Yang, J.; Liu, L. Trickle Flow Aided Atomic Layer Deposition (ALD) Strategy for Ultrathin Molybdenum Disulfide ($MoS_{2)}$ Synthesis. *ACS Appl. Mater. Inter.* **2019**, *11*, 36270-36277.

(16) Yang, J.; Liu, L. Trickle Flow Aided Atomic Layer Deposition (ALD) Strategy for Ultrathin Molybdenum Disulfide (MoS_2) Synthesis. *ACS Appl. Mater. Inter.* **2019**, *11*, 36270-36277.

(17) Li, H.; Zhang, Q.; Yap, C. C. R.; Tay, B. K.; Edwin, T. H. T.; Olivier, A.; Baillargeat, D. From Bulk to Monolayer MoS_2: Evolution of Raman Scattering. *Adv. Funct. Mater.* **2012**, *22*, 1385-1390.

(18) Lee, C.; Yan, H.; Brus, L. E.; Heinz, T. F.; Hone, J.; Ryu, S. Anomalous Lattice Vibrations of Single- and Few-Layer MoS_2. *ACS Nano* **2010**, *4*, 2695-2700.

(19) Mackus, A. J. M.; Schneider, J. R.; MacIsaac, C.; Baker, J. G.; Bent, S. F. Synthesis of Doped, Ternary, and Quaternary Materials by Atomic Layer Deposition:

A Review. *Chem. Mater.* **2019**, *31*, 1142-1183.

(20) Jeon, W.; Cho, Y.; Jo, S.; Ahn, J.; Jeong, S. Wafer-Scale Synthesis of Reliable High-Mobility Molybdenum Disulfide Thin Films via Inhibitor-Utilizing Atomic Layer Deposition. *Adv. Mater.* **2017**, *29*, 1703031-1703039.

(21) Tongay, S.; Sahin, H.; Ko, C.; Luce, A.; Fan, W.; Liu, K.; Zhou, J.; Huang, Y.; Ho, C.; Yan, J.et al. Monolayer behaviour in bulk ReS_2 due to electronic and vibrational decoupling. *Nat. Commun.* **2014**, *5*, 4252-4258.

(22) Sneha, V. R.; Padma, N.; Yadav, R. A.; Jagannath; Girija, K. G.; Arvind, A.; Rao, R. Interlayer coupling and diode characteristics of heterostructures of solution processed MoS_2:ReS_2 nanocrystals. *Appl. Surf. Sci.* **2020**, *505*, 144475-144486.

(23) Zhao, M.; Zhang, W.; Liu, M.; Zou, C.; Yang, K.; Yang, Y.; Dong, Y.; Zhang, L.; Huang, S. Interlayer coupling in anisotropic/isotropic van der Waals heterostructures of ReS_2 and MoS_2 monolayers. *Nano Res.* **2016**, *9*, 3772-3780.

(24) Zhang, T.; Jiang, B.; Xu, Z.; Mendes, R. G.; Xiao, Y.; Chen, L.; Fang, L.; Gemming, T.; Chen, S.; Rűmmeli, M. H.et al. Twinned growth behaviour of two-dimensional materials. *Nat. Commun.* **2016**, 7, 13911-13918.

(25) Jiao, Y.; Hafez, A. M.; Cao, D.; Mukhopadhyay, A.; Ma, Y.; Zhu, H. Metallic MoS_2 for High Performance Energy Storage and Energy Conversion. *Small* **2018**, *14*, 1800640-1800660.

(26) Lei, Z.; Zhan, J.; Tang, L.; Zhang, Y.; Wang, Y. Recent Development of Metallic (1T) Phase of Molybdenum Disulfide for Energy Conversion and Storage. *Adv. Energy Mater.* **2018**, *8*, 1703482-1703511.

(27) Wang, Z.; Luo, R.; Johnson, I.; Kashani, H.; Chen, M. Inlaid ReS_2 Quantum Dots in Monolayer MoS_2. *ACS Nano* **2020**, *14*, 899–906.

(28) Chakraborty, B.; Bera, A.; Muthu, D. V. S.; Bhowmick, S.; Waghmare, U. V.; Sood, A. K. Symmetry-dependent phonon renormalization in monolayer MoS_2 transistor. Phys. Rev. B **2016,** *85*, 161403-161407.

(29) Sreeparvathy, P. C.; Kanchana, V.; Anees, P.; Vaitheeswaran, G. Emergence of strain induced two dimensional metallic state in ReS_2. *J. Solid State Chem.* **2019**, *269*, 138-144.

(30) Guo, Y.; Robertson, J. Band engineering in transition metal dichalcogenides: Stacked versus lateral heterostructures. *Appl. Phys. Lett.* **2016**, *108*, 233104.

(31) Gehlmann, M.; Aguilera, I.; Bihlmayer, G.; Nemšák, S.; Nagler, P.; Gospodarič, P.; Zamborlini, G.; Eschbach, M.; Feyer, V.; Kronast, F.et al. Direct Observation of the Band Gap Transition in Atomically Thin ReS_2. *Nano Lett.* **2017**, *17*, 5187-5192.

(32) Froehlicher, G.; Lorchat, E.; Berciaud, S. Charge Versus Energy Transfer in Atomically Thin Graphene-Transition Metal Dichalcogenide van der Waals Heterostructures. *Phys. Rev. X* **2018**, *8*, 11007-11022.

(33) Shim, J.; Kang, D.; Kim, Y.; Kum, H.; Kong, W.; Bae, S.; Almansouri, I.; Lee, K.; Park, J.; Kim, J. Recent progress in Van der Waals (vdW) heterojunction-based electronic and optoelectronic devices. *Carbon* **2018**, *133*, 78-89.

(34) Chen, J.; Wu, Y.; Fu, C.; Cao, H.; Tan, X.; Shi, W.; Wu, Z. Ratiometric SERS biosensor for sensitive and reproducible detection of microRNA based on mismatched catalytic hairpin assembly. *Biosens. Bioelectron.* **2019**, *143*,

111619-111627.

(35) Wen, S.; Su, Y.; Dai, C.; Jia, J.; Fan, G.; Jiang, L.; Song, R.; Zhu, J. Plasmon Coupling-Enhanced Raman Sensing Platform Integrated with Exonuclease-Assisted Target Recycling Amplification for Ultrasensitive and Selective Detection of microRNA-21. *Anal. Chem.* **2019**, *91*, 12298-12306.

(36) Peng, L.; Yuan, Y.; Fu, X.; Fu, A.; Zhang, P.; Chai, Y.; Gan, X.; Yuan, R. Reversible and Distance-Controllable DNA Scissor: A Regenerated Electrochemiluminescence Biosensing Platform for Ultrasensitive Detection of MicroRNA. *Anal. Chem.* **2019**, *91*, 3239-3245.

(37) Shao, H.; Lin, H.; Lu, J.; Hu, Y.; Wang, S.; Huang, Y.; Guo, Z. Potential-resolved Faraday cage-type electrochemiluminescence biosensor for simultaneous determination of miRNAs using functionalized g-C3N4 and metal organic framework nanosheets. *Biosens. Bioelectron.* **2018**, *118*, 247-252.

(38) Fu, N.; Hu, Y.; Shi, S.; Ren, S.; Liu, W.; Su, S.; Zhao, B.; Weng, L. Au nanoparticles on two-dimensional MoS2 nanosheets as a photoanode for efficient photoelectrochemical miRNA detection. *Analyst* **2018**, 143, 1705-1712.

(39) Su, S.; Cao, W.; Liu, W.; Lu, Z.; Zhu, D.; Chao, J.; Weng, L.; Wang, L.; Fan, C.; Wang, L. Dual-mode electrochemical analysis of microRNA-21 using gold nanoparticle-decorated MoS_2 nanosheet. *Biosens. Bioelectron.* **2017**, *94*, 552-559.

(40) Sun, X.; Wang, H.; Jian, Y.; Lan, F.; Zhang, L.; Liu, H.; Ge, S.; Yu, J. Ultrasensitive microfluidic paper-based electrochemical/visual biosensor based on spherical-like cerium dioxide catalyst for miR-21 detection. *Biosens. Bioelectron.*

2018, *105*, 218-225.

(41) Wang, Y.; Shi, H.; Cui, K.; Zhang, L.; Ge, S.; Yan, M.; Yu, J. Hierarchical hematite/TiO_2 nanorod arrays coupled with responsive mesoporous silica nanomaterial for highly sensitive photoelectrochemical sensing. *Biosens. Bioelectron.* **2018**, *117*, 515-521.

(42) Yi, W.; Cai, R.; Xiang, D.; Wang, Y.; Zhang, M.; Ma, Q.; Cui, Y.; Bian, X. A novel photoelectrochemical strategy based on an integrative photoactive heterojunction nanomaterial and a redox cycling amplification system for ultrasensitive determination of microRNA in cells. *Biosens. Bioelectron.* **2019**, *143*, 111614-111620.

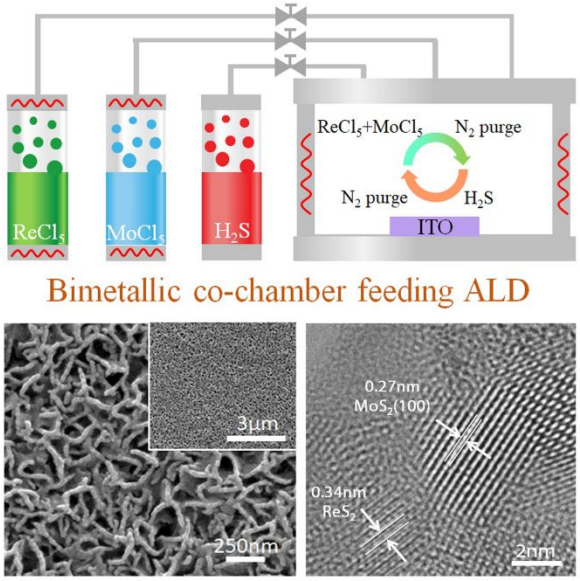

For Table of Contents Only

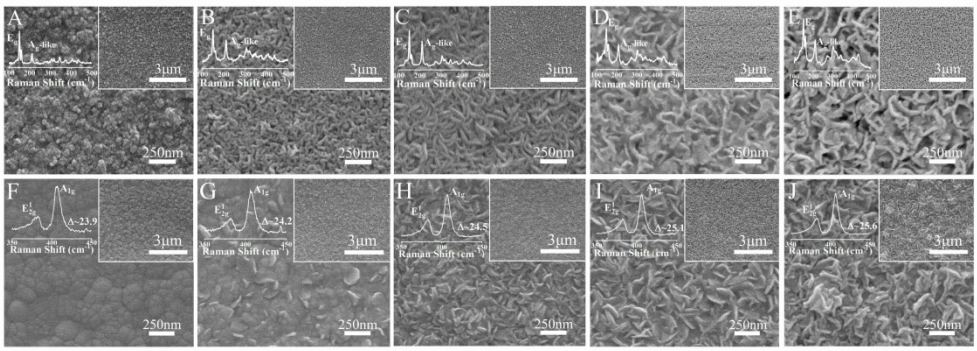

Figure 1. (A-E) SEM images of ReS2 films grown on ITO substrates obtained under 100, 150, 200, 250 and 300 ALD cycles; (F-J) SEM images of MoS2 films grown on ITO substrates obtained under 100, 150, 200, 250 and 300 ALD cycles. The insets in (A-J): the corresponding Raman spectra.

253x91mm (300 x 300 DPI)

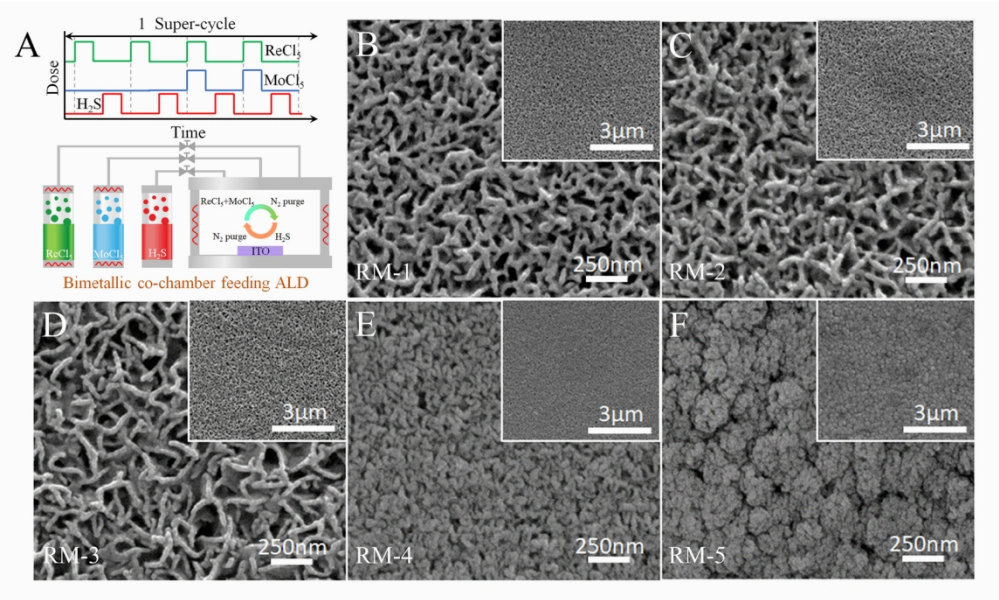

Figure 2. (A) Schematic images of a bimetallic co-chamber feeding ALD setup and the co-dosing ALD procedure for the preparation of MoS2-ReS2 heterojunctions. (B-F) SEM images of RM-1, RM-2, RM-3, RM-4, RM-5.

152x91mm (300 x 300 DPI)

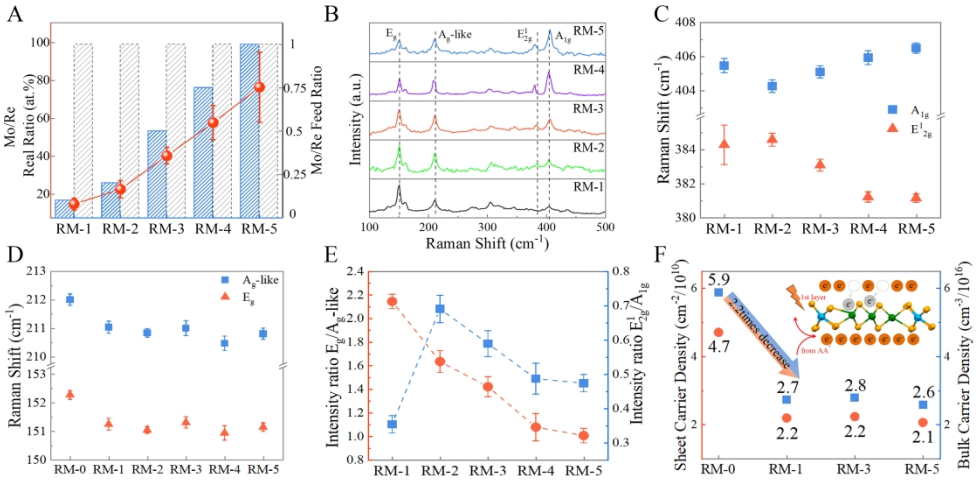

Figure 3. (A) The variation of the Mo-to-Re ratio for MoS2-ReS2 heterojunctions; (B) Raman spectra of different MoS2-ReS2 heterojunctions samples; (C) Evolution of peak positions of E12g and A1g modes in MoS2; (D) Evolution of peak positions of Eg and Ag-like modes in ReS2; (E) Evolution of E12g/A1g in MoS2 and Eg/Ag-like in ReS2 intensity ratio for different MoS2-ReS2 heterojunctions samples; (F) The carrier density of different MoS2-ReS2 heterojunctions samples tested in Hall measurement and inset shows the schematic of the electron-trapping effect caused by MoS2-ReS2 heterojunctions.

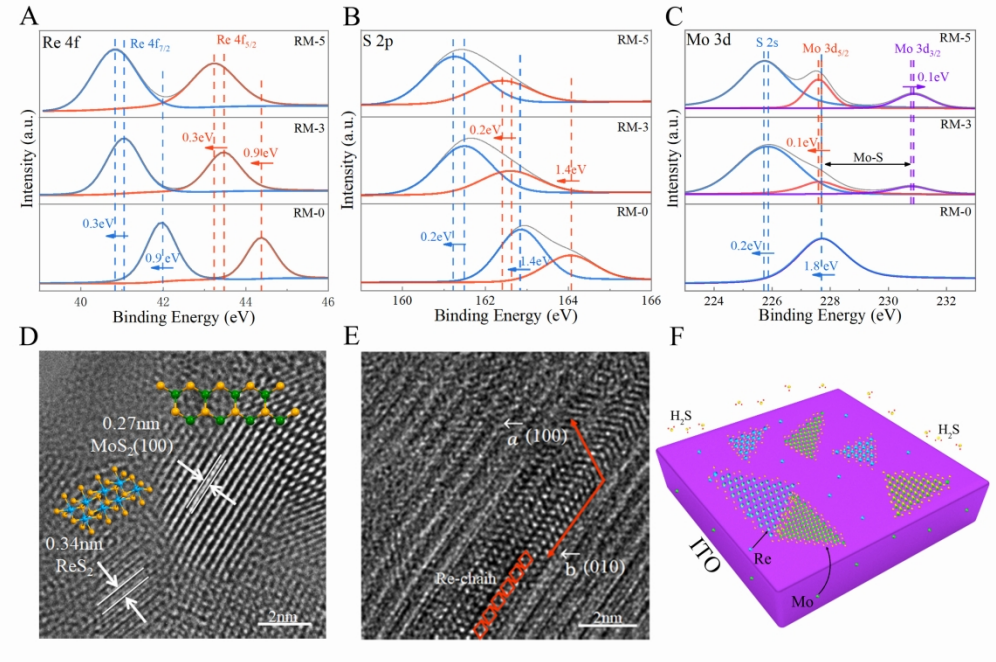

Figure 4. Re 4f (A), S 2p (B), Mo 3d (C) XPS spectra of ReS2 film and RM-3, RM-5. HR-TEM of MoS2-ReS2 heterojunctions (D) and ReS2 films (E). The schematic (F) for the MoS2-ReS2 heterojunctions prepared by bimetallic co-chamber feeding ALD.

254x169mm (300 x 300 DPI)

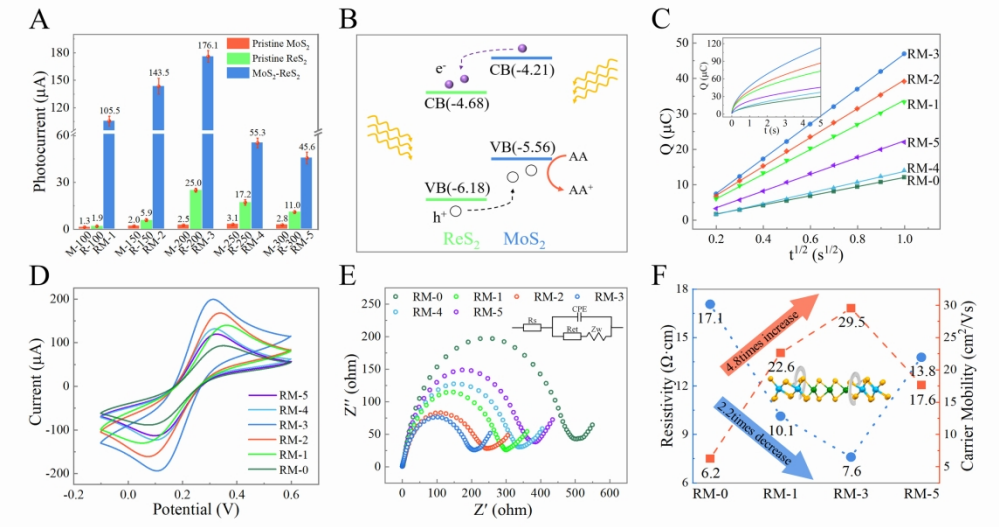

Figure 5. (A) The photocurrent response of pure MoS2, ReS2 with different ALD cycles and different heterojunction sample; (B) Schematic diagram of the band structure and charge transfer of MoS2-ReS2 heterojunctions; (C) The effective surface area, (D) CV and (E) EIS of pure MoS2, ReS2 and different heterojunction samples; (F) The resistivity and carrier mobility of different heterojunction samples tested in Hall measurement. Inset in (E): The schematic of equivalent circuit was consisted of solution resistance (Rs), electron-transfer resistance (Ret), constant-phase element (CPE), and Warburg impedance (Zw); Inset in (F): The metallic system caused by the stress at lattice junction.

254x134mm (300 x 300 DPI)

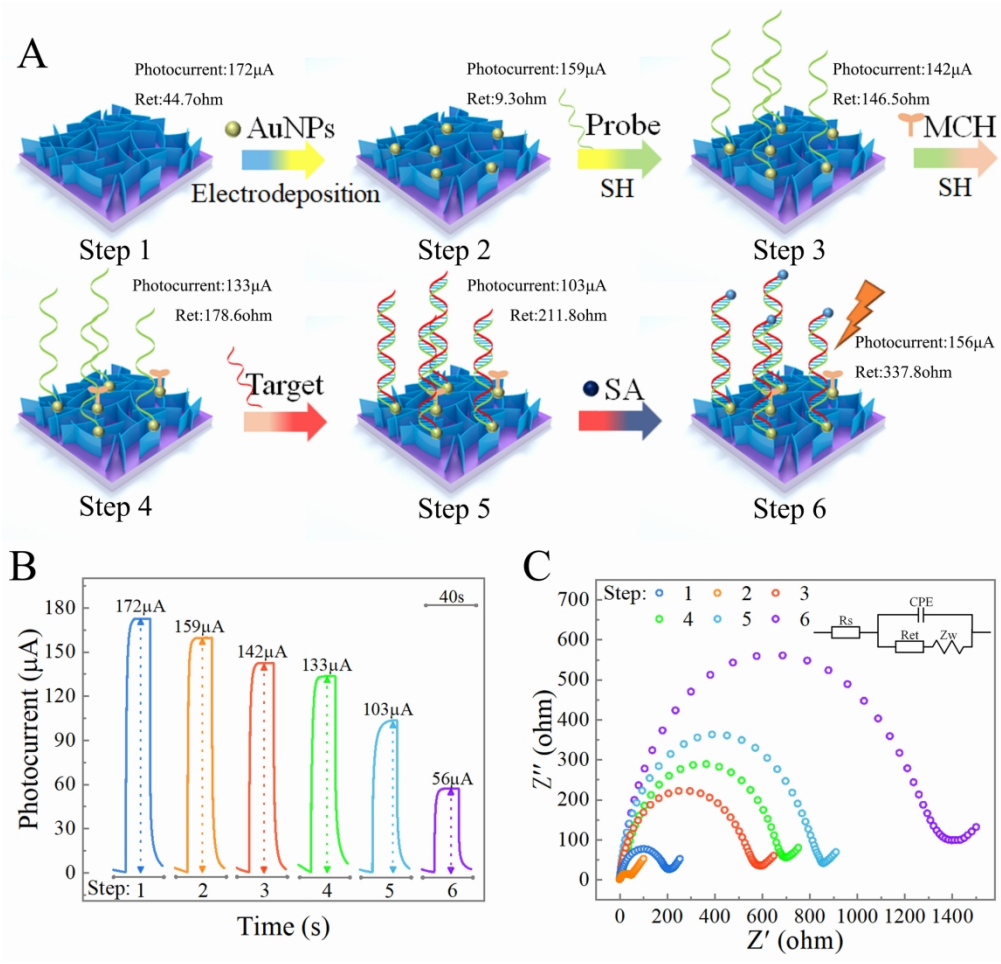

Figure 6. (A) Illustration of the proposed PEC biosensor for miRNA-21 Detection. (B, C) The photocurrent response and EIS images of different electrodes during the built of sensing platform, in which MoS2-ReS2/ITO, AuNPs/MoS2-ReS2/ITO, SH-DNA/AuNPs/MoS2-ReS2/ITO, MCH/SH-DNA/AuNPs/MoS2-ReS2/ITO, miRNA/MCH/SH-DNA/AuNPs/MoS2-ReS2/ITO, SA/miRNA/MCH/SH-DNA/AuNPs/MoS2-ReS2/ITO are step (1-6) respectively.

211x202mm (300 x 300 DPI)

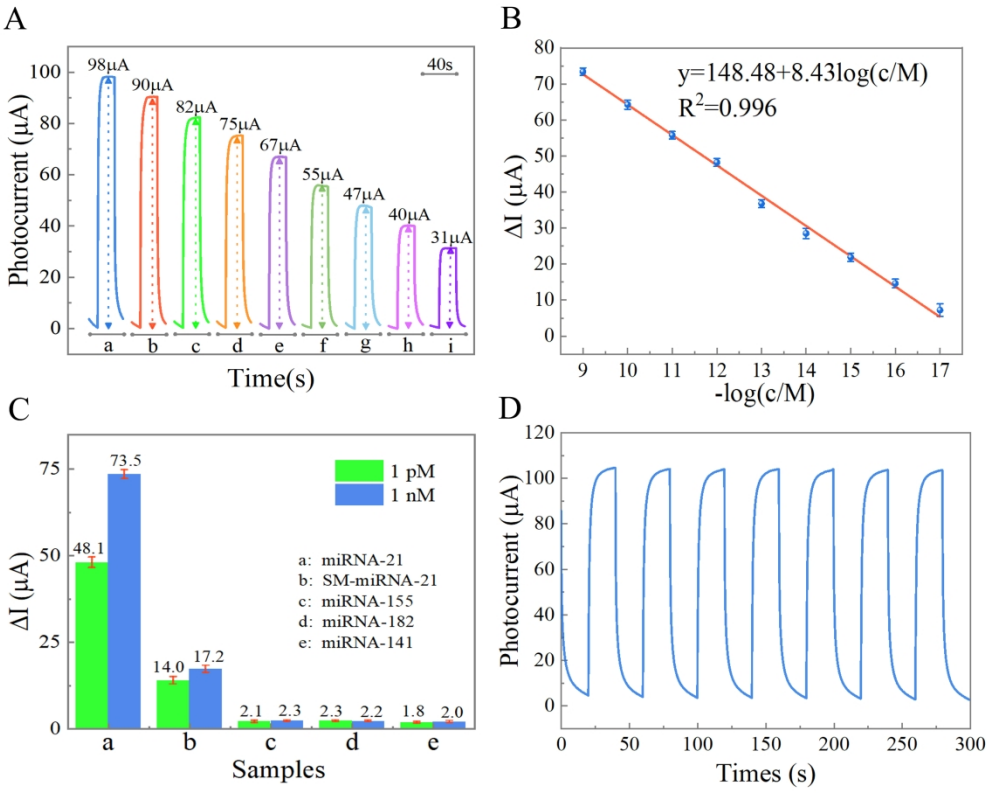

Figure 7. (A) Photocurrent response to different concentrations of miRNA-21 from (a)-(i): 10 aM, 100 aM, 1 fM, 10 fM, 100 fM, 1 pM, 10 pM, 100 pM, 1 nM. (B) The calibration curve of the photocurrent versus logarithm value of miRNA-21 concentration. Error bars = standard deviations (n =5). (C) The selectivity of the sensing platform hybridized to 1 pM and 1 nM miRNA-21 (a), single-base mismatch miRNA-21 (b), miRNA-155 (c), miRNA-182 (d) and miRNA-141 (e). (D) The stability of the photocurrent response in 0.1 M PBS solution containing 0.1 M AA with light on and off.

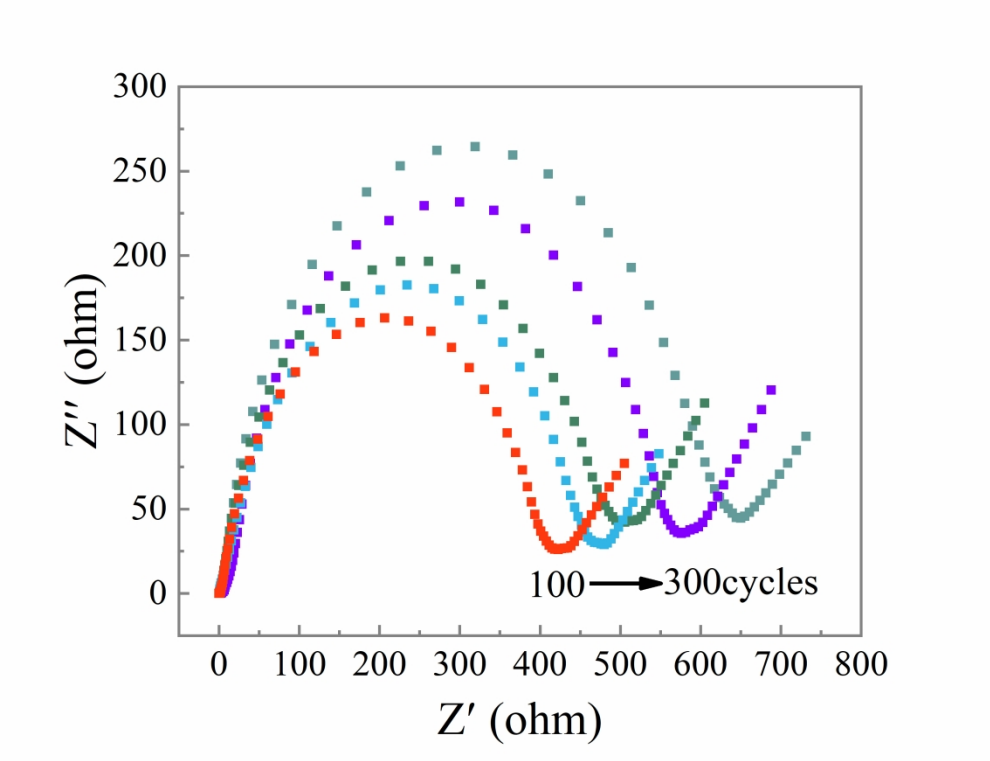

Figure S1. The EIS diagram of ReS2 grown under 100, 150, 200, 250, 300 ALD cycles.

272x208mm (300 x 300 DPI)

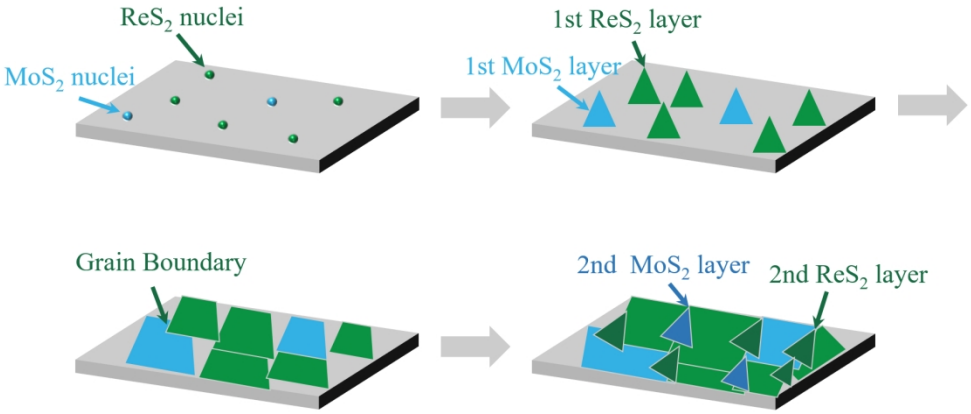

Figure S2. The growth mechanism of bimetallic co-chamber feeding ALD.

160x70mm (300 x 300 DPI)

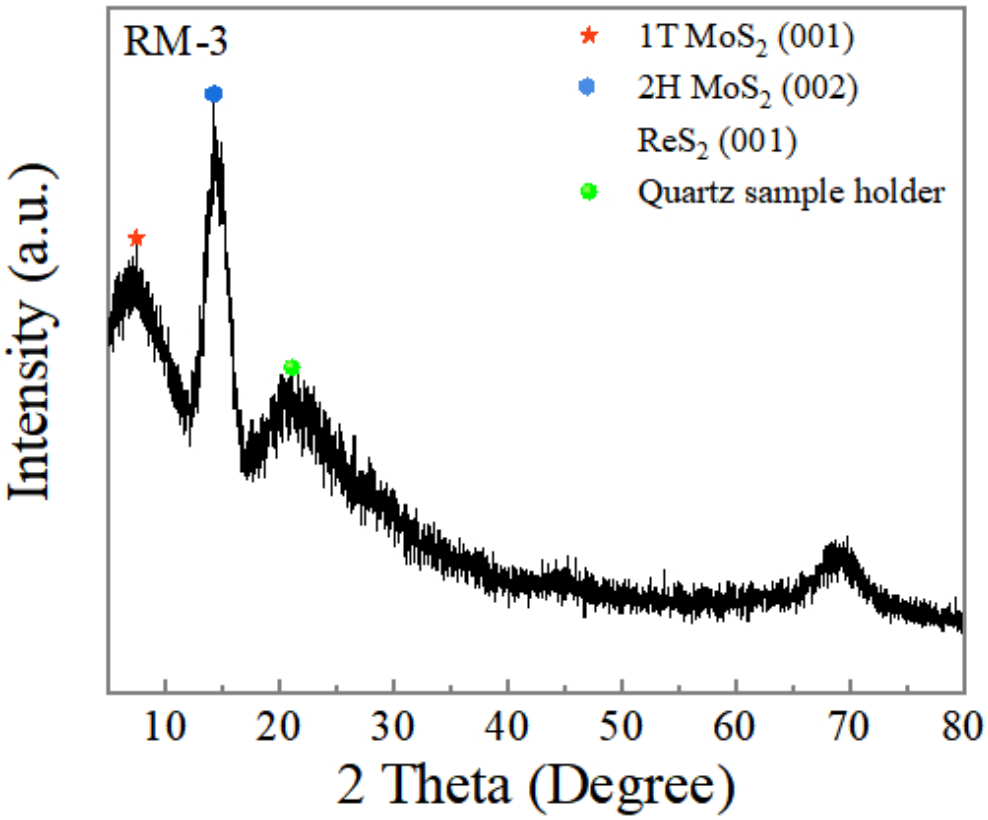

Figure S3. X-ray diffraction spectra of RM-3.

43x35mm (300 x 300 DPI)

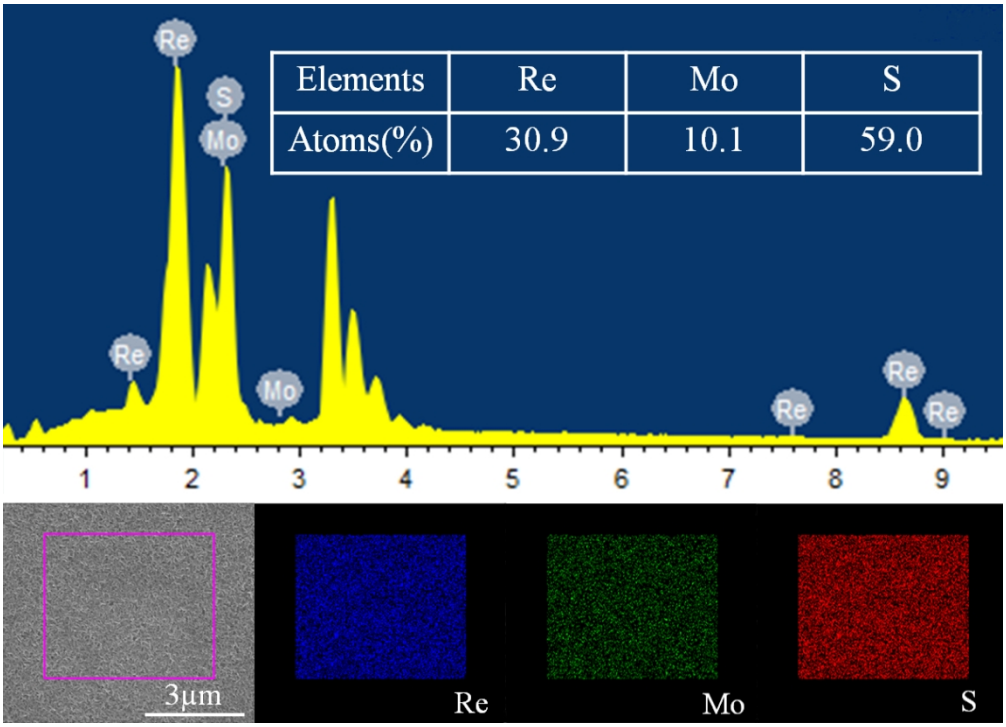

Figure S4. The EDS elements mapping of RM-3.

102x73mm (300 x 300 DPI)

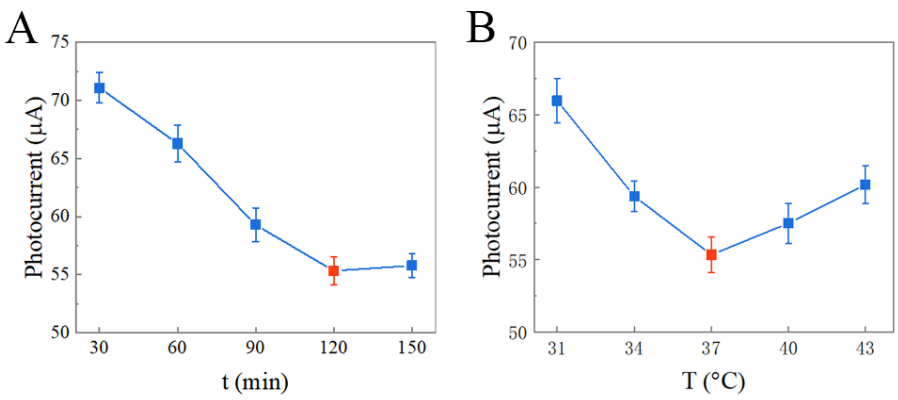

Figure S5. Parameter optimization of incubation temperature and hybridization time.

90x39mm (300 x 300 DPI)

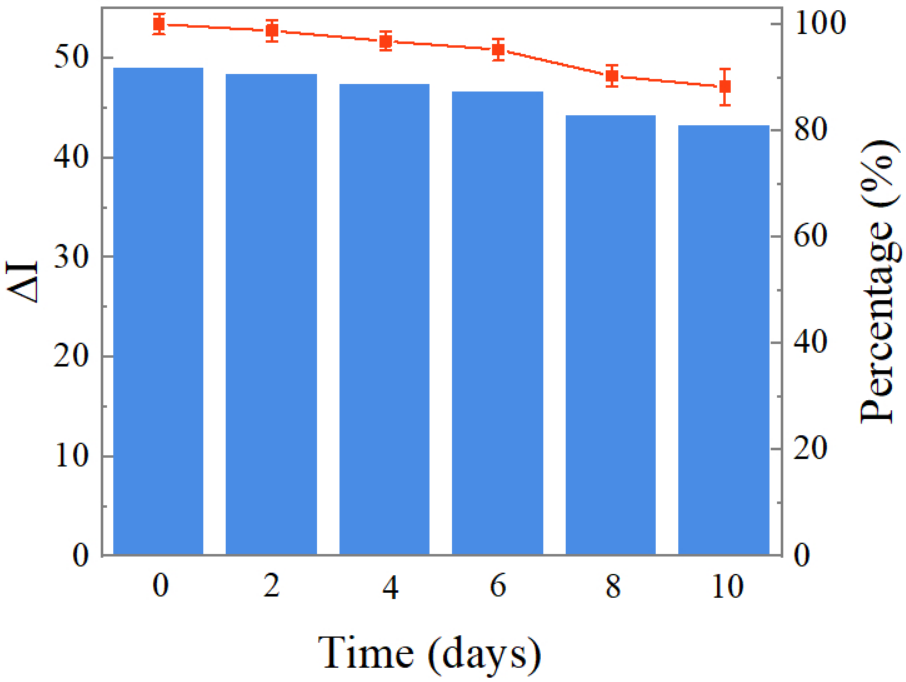

Figure S6. The long-term stability of proposed biosensor.

67x51mm (300 x 300 DPI)

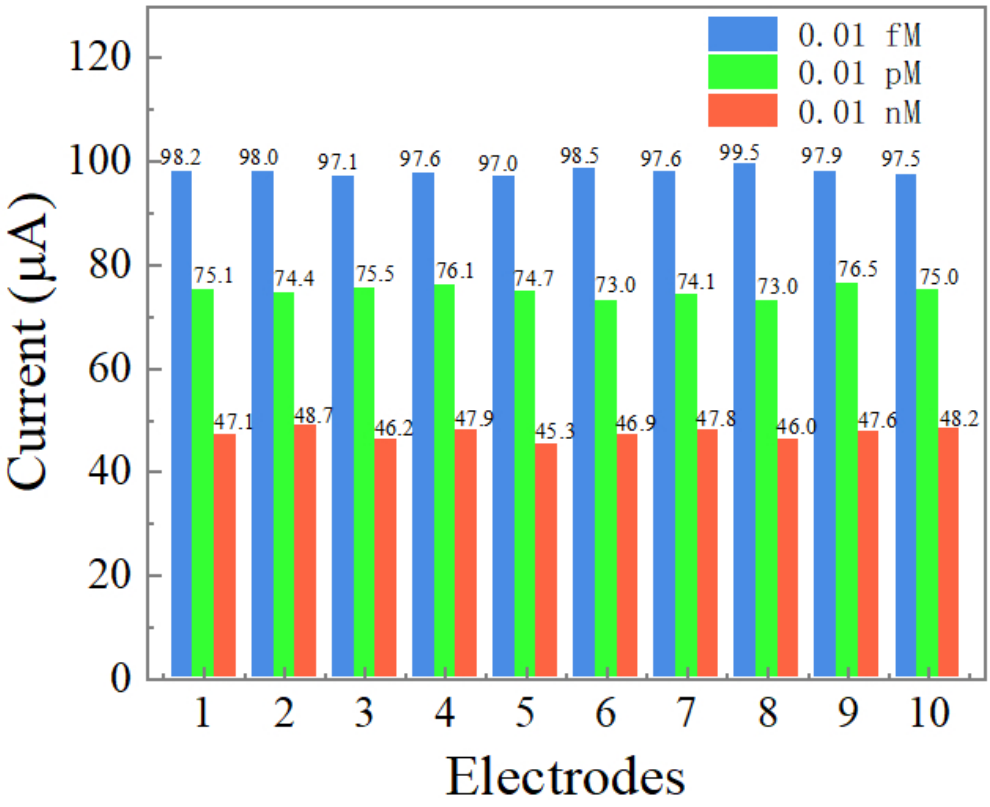

Figure S7. Current responses of ten equally prepared electrodes for 0.01 fM, 0.01 pM and 0.01 nM miRNA-21 detections.

53x43mm (300 x 300 DPI)

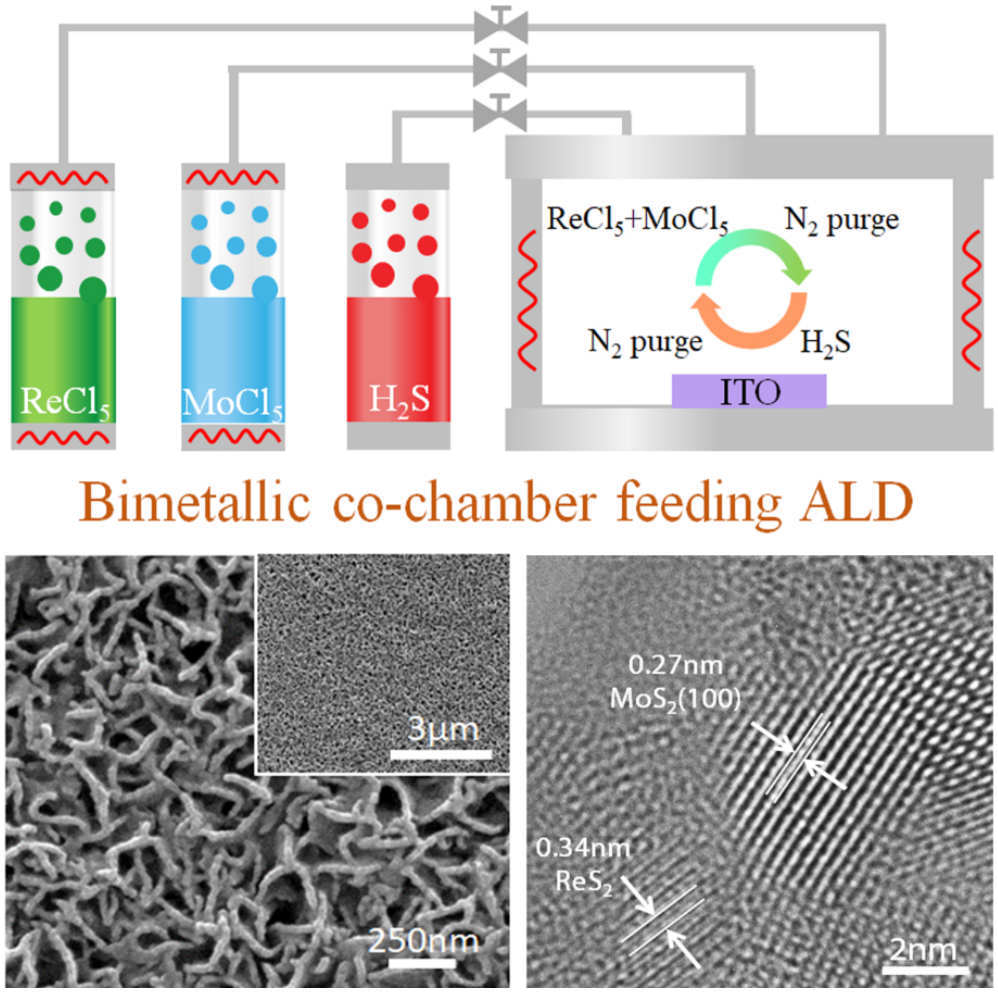

TOC

243x242mm (96 x 96 DPI)